iScience

CellPress
OPEN ACCESS

Article

# A resource of high-quality and versatile nanobodies for drug delivery

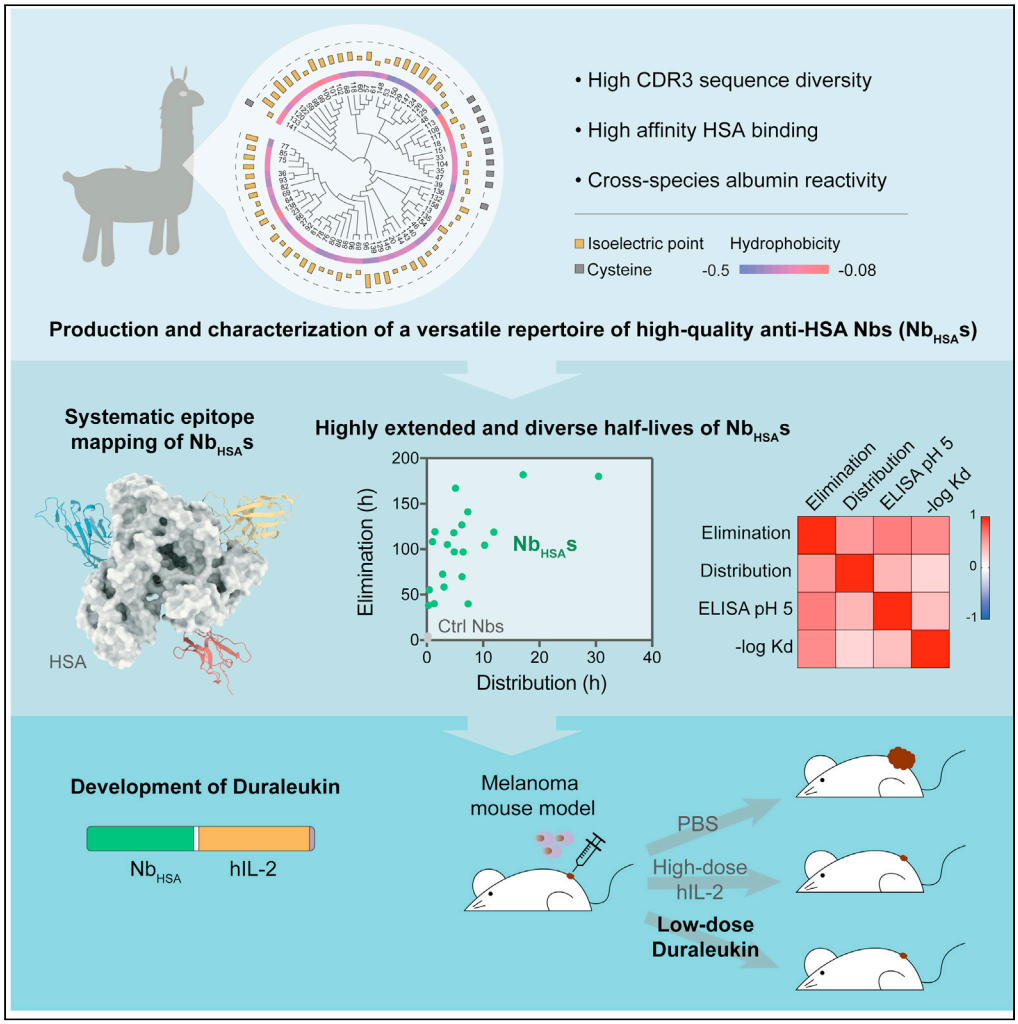


Zhuolun Shen, Yufei Xiang, Sandra Vergara, ..., Guillermo Calero, Baoli Hu, Yi Shi

yi.shi@pitt.edu

## Highlights

We provide a resource of high-affinity and versatile albumin nanobodies for drug delivery

We systematically map albumin nanobody epitopes by hybrid structural approaches

We parallelly measure the pharmacokinetics of nanobodies in a humanized mouse model

We develop nanobody-cytokine conjugates "Duraleukin" for cancer immunotherapy

Shen et al., iScience 24, 103014
September 24, 2021 
https://doi.org/10.1016/j.isci.2021.103014

iScience

CellPress
OPEN ACCESS

Article

# A resource of high-quality and versatile nanobodies for drug delivery

Zhuolun Shen,[1,7] Yufei Xiang,[1] Sandra Vergara,[2] Apeng Chen,[3,4] Zhengyun Xiao,[1] Ulises Santiago,[6] Changzhong Jin,[1] Zhe Sang,[1,8] Jiadi Luo,[5] Kong Chen,[5] Dina Schneidman-Duhovny,[9] Carlos Camacho,[6] Guillermo Calero,[2] Baoli Hu,[3,4,10] and Yi Shi[1,8,11,*]

## SUMMARY

**Therapeutic and diagnostic efficacies of small biomolecules and chemical compounds are hampered by suboptimal pharmacokinetics. Here, we developed a repertoire of robust and high-affinity antihuman serum albumin nanobodies ($Nb_{HSA}$) that can be readily fused to small biologics for half-life extension. We characterized the thermostability, binding kinetics, and cross-species reactivity of $Nb_{HSA}$s, mapped their epitopes, and structurally resolved a tetrameric HSA-Nb complex. We parallelly determined the half-lives of a cohort of selected $Nb_{HSA}$s in an HSA mouse model by quantitative proteomics. Compared to short-lived control nanobodies, the half-lives of $Nb_{HSA}$s were drastically prolonged by 771-fold. $Nb_{HSA}$s have distinct and diverse pharmacokinetics, positively correlating with their albumin binding affinities at the endosomal pH. We then generated stable and highly bioactive $Nb_{HSA}$-cytokine fusion constructs "Duraleukin" and demonstrated Duraleukin's high preclinical efficacy for cancer treatment in a melanoma model. This high-quality and versatile Nb toolkit will help tailor drug half-life to specific medical needs.**

## INTRODUCTION

Chemical compounds and small biomolecules (<50 kDa) are known to be rapidly eliminated in the plasma (from min to h) by glomerular filtration. Such poor pharmacokinetics has greatly limited the efficacy of numerous clinically important peptides and small proteins including hormones, cytokines, coagulation factors, and antibody fragments such as nanobodies (Nbs). Various strategies have been developed to improve the half-lives of the target biomolecules. These include chemical modifications by PEGylation, fusion with an antibody Fc domain, and piggy-back delivery by targeting serum albumin (Czajkowsky et al., 2012; Harris and Chess, 2003; Kratz, 2008; Larsen et al., 2016). Human serum albumin (HSA) is a highly abundant blood protein with a long plasma half-life of approximately three weeks (Larsen et al., 2016). HSA has a molecular weight of ~67 kDa and is refractory to renal filtration. Moreover, it can bind to the neonatal Fc receptor (FcRn) that is ubiquitously expressed in various cell types. This interaction requires the endosomal pH (<pH 6.5) and is critical for the FcRn-mediated transcytosis of albumin that prevents its endolysosomal degradation to substantially improve albumin's half-life (Merlot et al., 2014; Sand et al., 2015). Although HSA is the most abundant serum protein, its intracellular concentration is likely very low (Merlot et al., 2014; Peters, 1996).

The high serum concentration and the exceptionally long *in vivo* half-life make HSA an excellent trojan horse for drug delivery. Different albumin-based approaches have been developed including direct fusion to HSA and development of albumin nanoparticles as well as albumin-binding domains (ABDs) derived from gram-positive bacteria to improve the pharmacokinetics of target therapeutics (Larsen et al., 2016; Merlot et al., 2014; Sleep et al., 2013). Despite these advances, however, successful preclinical and clinical applications of these technologies remain limited (Kontermann, 2016). Development of robust, highly specific and cost-effective new HSA binders, ideally with inherent low immunogenicity, high bioavailability, and versatility in modulating pharmacokinetic properties based on specific medical needs remains highly desirable.

Nbs are robust and small antigen-binding fragments (~15 kDa) that are derived from camelid's heavy-chain-only antibodies (HcAbs) (Hamers-Casterman et al., 1993). They are characterized by marked

[1]Department of Cell Biology, University of Pittsburgh, Pittsburgh, PA, USA

[2]Department of Structural Biology, University of Pittsburgh, Pittsburgh, PA, USA

[3]Department of Neurological Surgery, University of Pittsburgh, Pittsburgh, PA, USA

[4]Pediatric Neurosurgery, UPMC Children's Hospital of Pittsburgh, Pittsburgh, PA, USA

[5]Department of Medicine, University of Pittsburgh, Pittsburgh, PA, USA

[6]Department of Computational and Systems Biology, University of Pittsburgh, Pittsburgh, PA, USA

[7]School of Medicine, Tsinghua University, Beijing, China

[8]University of Pittsburgh-Carnegie Mellon University Joint Program for Computational Biology, Pittsburgh, PA, USA

[9]School of Computer Science and Engineering, Institute of Life Sciences, University of Jerusalem, Tambaram, Israel

[10]Molecular and Cellular Cancer Biology Program, UPMC Hillman Cancer Center, Pittsburgh, PA, USA

[11]Lead contact

*Correspondence: yi.shi@pitt.edu

https://doi.org/10.1016/j.isci.2021.103014

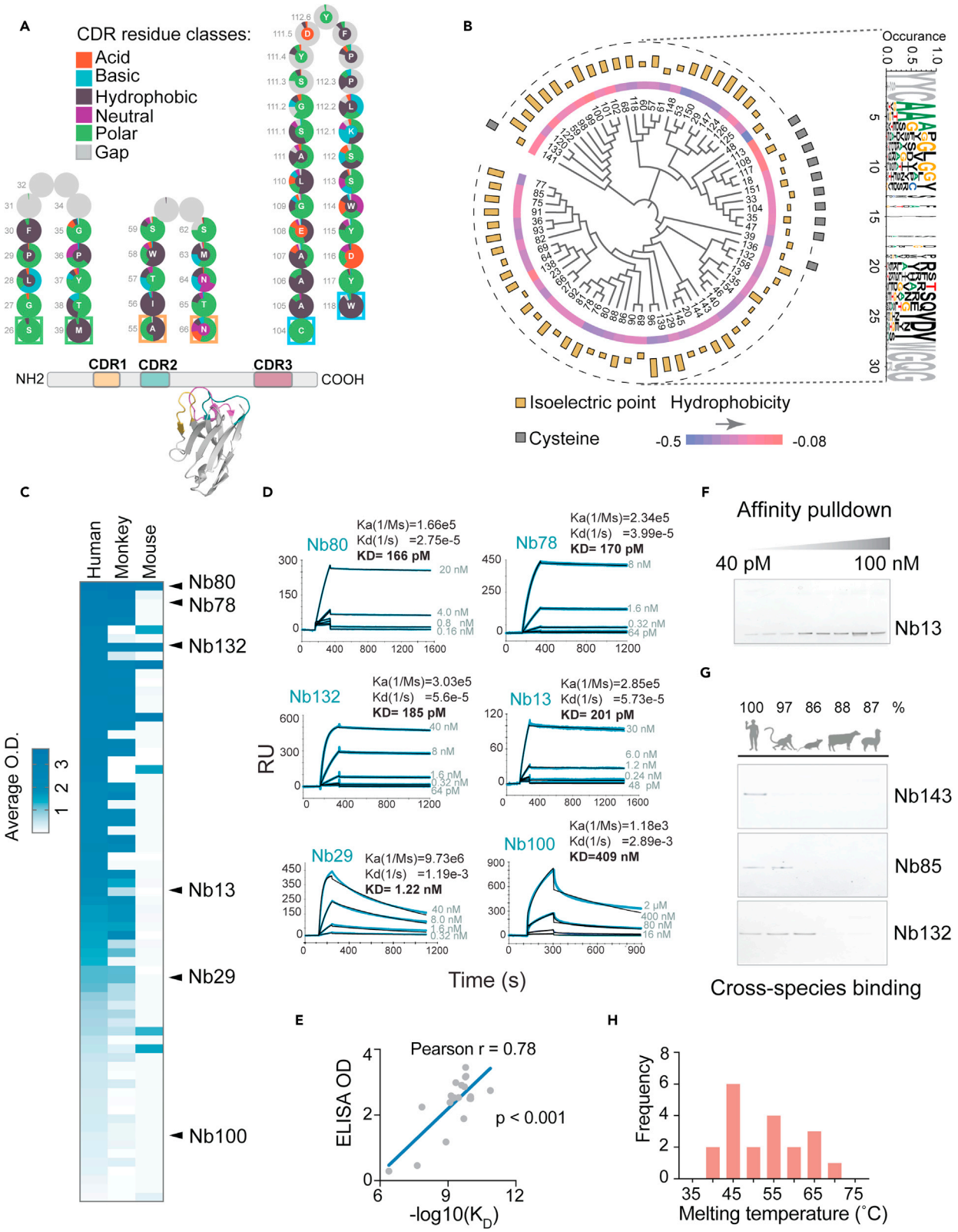
A
CDR residue classes:
Acid
Basic
Hydrophobic
Neutral
Polar
Gap
CDR1
CDR2
CDR3
NH2
COOH
B
Occurance
Isoelectric point
Hydrophobicity
Cysteine
-0.5
-0.08
C
Human
Monkey
Mouse
Nb80
Nb78
Nb132
Nb13
Nb29
Nb100
Average O.D.
D
Nb80
Ka(1/Ms)=1.66e5
Kd(1/s) =2.75e-5
KD= 166 pM
Nb78
Ka(1/Ms)=2.34e5
Kd(1/s) =3.99e-5
KD= 170 pM
Nb132
Ka(1/Ms)=3.03e5
Kd(1/s) =5.6e-5
KD= 185 pM
Nb13
Ka(1/Ms)=2.85e5
Kd(1/s) =5.73e-5
KD= 201 pM
Nb29
Ka(1/Ms)=9.73e6
Kd(1/s) =1.19e-3
KD= 1.22 nM
Nb100
Ka(1/Ms)=1.18e3
Kd(1/s) =2.89e-3
KD=409 nM
RU
Time (s)
E
Pearson r = 0.78
p < 0.001
ELISA OD
-log10(K_D)
F
Affinity pulldown
40 pM
100 nM
Nb13
G
100 97 86 88 87 %
Nb143
Nb85
Nb132
Cross-species binding
H
Frequency
Melting temperature (˚C)

**Figure 1. Identification and characterization of $Nb_{HSA}$**

(A) Schematic structure and amino acid composition of $Nb_{HSA}$. 71 different Nbs were analyzed by Yvis. The amino acid frequency at each CDR position was calculated. Amino acids were color-coded and classified based on the physicochemical properties.

(B) Circos and sequence logo plots showing the diversity of CDR3.

(C) ELISA heat map of albumin cross-species binding of 71 different Nbs.

(D) Binding kinetics of 6 Nbs by SPR (surface plasmon resonance).

(E) Correlation between ELISA O.D. (optical density) and SPR $K_D$ affinity.

(F) Immunoprecipitation of the HSA-$Nb_{13}$ complex at different concentrations of $Nb_{13}$.

(G) Validation of Nb cross-species reactivity by immunoprecipitation. Three Nbs ($Nb_{143}$, $Nb_{85}$, and $Nb_{132}$) were immunoprecipitated by affinity resins coupled with albumin of different species, including human, monkey, mouse, bovine, and llama.

(H) The plot of the thermostability of 20 $Nb_{HSA}$ selected for measurement by differential scanning fluorimetry.

physiochemical properties including high solubility and stability (Xiang et al., 2020a, 2021). Nbs can be rapidly produced in microbes such as *Escherichia coli* and yeast cells at low costs. Because of the small size and robustness, Nbs have fast tissue distributions and high bioavailability for *in vivo* therapeutic and diagnostic applications (Jovčevska and Muyldermans, 2020; Kijanka et al., 2015). Monomeric Nbs can be easily bioengineered into multivalent forms to improve binding affinities and bioactivities (Fridy et al., 2014; Harmsen and De Haard, 2007; Xiang et al., 2020a, 2021). Importantly, camelid Nbs have high sequence and structural similarity with human IgG heavy chains (Kijanka et al., 2015; Vincke et al., 2009). To date, over 35 clinical trials have been conducted on more than 1,000 patients and healthy volunteers, revealing high biosafety of Nbs in humans. In addition, the first Nb drug (caplacizumab) has recently been approved by the FDA (Scully et al., 2019). Stable Nbs are flexible for administration including direct inhalation therapy by Nb aerosols, making their use against respiratory viruses very appealing (Cunningham et al., 2021; Larios Mora et al., 2018; Liang et al., 2020; Nambulli et al., 2021; Patton and Byron, 2007; Van Heeke et al., 2017).

Recently, we have developed a robust proteomic technology for large-scale identification and affinity classification of drug-quality Nbs (*28*). Using this pipeline, we identified thousands of high-affinity anti-HSA Nbs ($Nb_{HSA}$) (Xiang et al., 2021). In this study, we produced and systematically characterized a repertoire of structurally diverse and sub-nM affinity $Nb_{HSA}$s for drug delivery. We developed a multiplexed pharmacokinetic assay by quantitative proteomics and determined the half-lives of dozens of selected $Nb_{HSA}$s in an $Alb^{-/-}$ FcRn-humanized mouse model (B6.Cg-Tg(FCGRT)32Dcr *Alb*$^{em12Mvw}$ *Fcgrt*$^{tm1Dcr}$/MvwJ) (Roopenian et al., 2015). Our analysis reveals that $Nb_{HSA}$s have distinct and diverse pharmacokinetic profiles with highly extended half-lives ranging from 1.6 to 7.6 days in the HSA model. The half-lives of $Nb_{HSA}$ positively correlate with their albumin binding affinities at the mildly acidic pH. To demonstrate the utility of our $Nb_{HSA}$s, we generated "Duraleukin" by fusing several cross-species $Nb_{HSA}$s to human interleukin-2 (hIL-2) – a small anticancer cytokine whose clinical efficacy has been substantially compromised by its small size and short serum half-life. Duraleukin can be rapidly produced from *E. coli* cells and have excellent stability and bioactivity. Using a melanoma mouse model, we demonstrated the high preclinical efficacy of Duraleukin for cancer treatment. This versatile and well-characterized Nb resource is shared with the research community to help advance biomedical discoveries into therapeutic development.

## RESULTS

### Characterization of a repertoire of high-quality $Nb_{HSA}$

We hypothesize that the *in vivo* half-lives of $Nb_{HSA}$s are related to their biophysical (such as binding kinetics, solubility, stability, etc.) and structural properties (Ovacik and Lin, 2018). To maximize these properties, we included a collection of ~90 $Nb_{HSA}$s with highly diverse complementarity-determining region (CDR) 3 sequences, which form hypervariable loop structures (fingerprints) for specific antigen binding. As shown in Figure 1B, the CDR3s of these highly selected Nbs vary substantially in amino acid composition, sequence length, isoelectric point (pI), and hydrophobicity. To produce recombinant Nbs, their amino acid sequences were reverse translated into DNA fragments (~350 bp), which were subsequently synthesized and cloned into a his6-tag vector (pET-21) for recombinant protein production in *E. coli*. As expected, the majority of Nbs (71/90) were highly soluble and can be rapidly purified by the His-cobalt affinity resin (Figure 1A; Data S1).

To assess binding and cross-species reactivity of our $Nb_{HSA}$s, we performed the enzyme-linked immunosorbent assay (ELISA) for serum albumins from five different species including human, nonhuman primate (NHP, cynomolgus monkey), rodent (mouse), bovine (cow), and camelid (llama). Optical density (O.D.) values were

calculated from the ELISA curves to generate a heat map that summarizes the binding results (Figure 1C). Our data confirm that all selected $Nb_{HSA}$s can bind strongly to HSA. Around three quarters (53/71) of $Nb_{HSA}$s bind monkey albumin and 11% of them (8/71) can also interact with mouse albumin. These results likely reflect the high sequence similarity (92%) between HSA and cynomolgus monkey albumin and relatively poor residue conservation (78%) between HSA and mouse albumin. Interestingly, we identified six $Nb_{HSA}$s that bind all (Figure 1C; STAR methods) but llama and bovine albumins (Figure 1G). These Nbs may target relatively conserved epitopes specifically shared among HSA, NHP, and mouse albumins. C ross-species Nbs will be highly useful in the translation of preclinical studies in the animal models into clinal trials.

To measure the binding kinetics of $Nb_{HSA}$s, we selected 20 $Nb_{HSA}$s for surface plasmon resonance (SPR) analysis (Figures 1C, 1D, and S1). Three quarters (15/20) of $Nb_{HSA}$s bind extremely tight to HSA with sub-nanomolar affinities. The remaining $Nb_{HSA}$s span single digit to hundreds of nanomolar affinities for HSA binding (Figure S1). Consistent with the previous report (Heinrich et al., 2010), we found that ELISA O.D. correlates well with the SPR affinity (Pearson $r = 0.78$, $p < 0.001$) (Figure 1E) and can be used to approximate binding affinity.

Next, we assess the thermostability of a cohort of representative $Nb_{HSA}$s by differential scanning fluorimetry (Niesen et al., 2007). While Nbs were produced from *E. coli* whole-cell lysis, they remain stable with melting temperatures ($T_m$) ranging between ~39°C and 70°C (Figures 1H and S2; Data S2). The thermostability could be further improved by using periplasmic preparations (Pleiner et al., 2015). In summary, our highly selected $Nb_{HSA}$s are characterized by marked physicochemical properties such as high solubility and stability, which are critical for drug development, storage, and delivery (Carter, 2006; Holliger and Hudson, 2005).

## Epitope mapping by structural proteomics

Epitope mapping can provide insights into how Nbs uniquely bind the target with high affinity and selectivity and may guide the rationale design of therapeutics such as chemical compounds and small peptides/proteins for HSA binding (D Brooks, 2014; Flyak et al., 2018; Nivarthi et al., 2017). To systematically map Nb epitopes, we used a hybrid approach that integrates chemical cross-linking/mass spectrometry (CXMS) and structural modeling for high-throughput structural analysis. CXMS identifies short cross-links at amino acid resolution, which can be used as spatial restraints (molecular rulers) to calculate structural models to help map binding interfaces (Chait et al., 2016; Rout and Sali, 2019; Russel et al., 2012; Shi et al., 2014, 2015; Xiang et al., 2020b; Yu and Huang, 2018).

Thirty-eight HSA-Nb complexes were reconstituted *in vitro* and cross-linked by disuccinimidyl suberate, which can reach up to 30 Å between two cross-linked amines (e.g., lysine residues). After cross-linking, the complexes were separated by SDS-PAGE, in-gel digested, and the resulting cross-linked peptides were analyzed by liquid chromatography coupled to mass spectrometry (LC/MS) (STAR methods). A total of 125 intersubunit cross-links were confidently identified by MS (Data S3) and were used to compute the models (STAR methods). 29 HSA-Nb complex models converged with an average root mean square deviation (RMSD) of 7.4 Å (Figure 2C). The majority (87.5%) of cross-links were satisfied by the models (Figure S3B).

Previously, X-ray crystallographic analysis revealed three domains of HSA (I, II, and III). Each domain is composed of two subdomain structures. In addition, domains II and III are characterized by a small pocket composed of hydrophobic and positively charged residues that allow binding of specific metabolites and chemical compounds (Sudlow's sites) (Ghuman et al., 2005; Sudlow et al., 1975; Sugio et al., 1999). Our analysis identified six distinct Nb epitope clusters (clusters A to F) (Figure 2A; Data S3). More than three-quarters of Nbs bind two major epitope clusters (A: 31% and E: 44.8%) (Figure 2B). The rest (B, C, D and F) bind four minor clusters. Moreover, cluster A Nbs bind epitopes between domains I and II of HSA. Cluster B also targets these domains but localizes on the opposite side of A. Cluster C binds domain I, while the other three epitope clusters (D, E, and F) mainly target domain III. Noticeably, two dominant clusters of A and E overlap substantially with Sudlow's site I and II, respectively. Moreover, our models indicate that high-affinity Nbs mainly bind concave epitopes (Figure 2D). Critically, most of our $Nb_{HSA}$s do not target the major crevice of HSA which is essential for FcRn binding (Figure S3A). The only exception is $Nb_{126}$, which based on our structural model, can interfere with the HSA-FcRn interaction and therefore may have inferior pharmacokinetics.

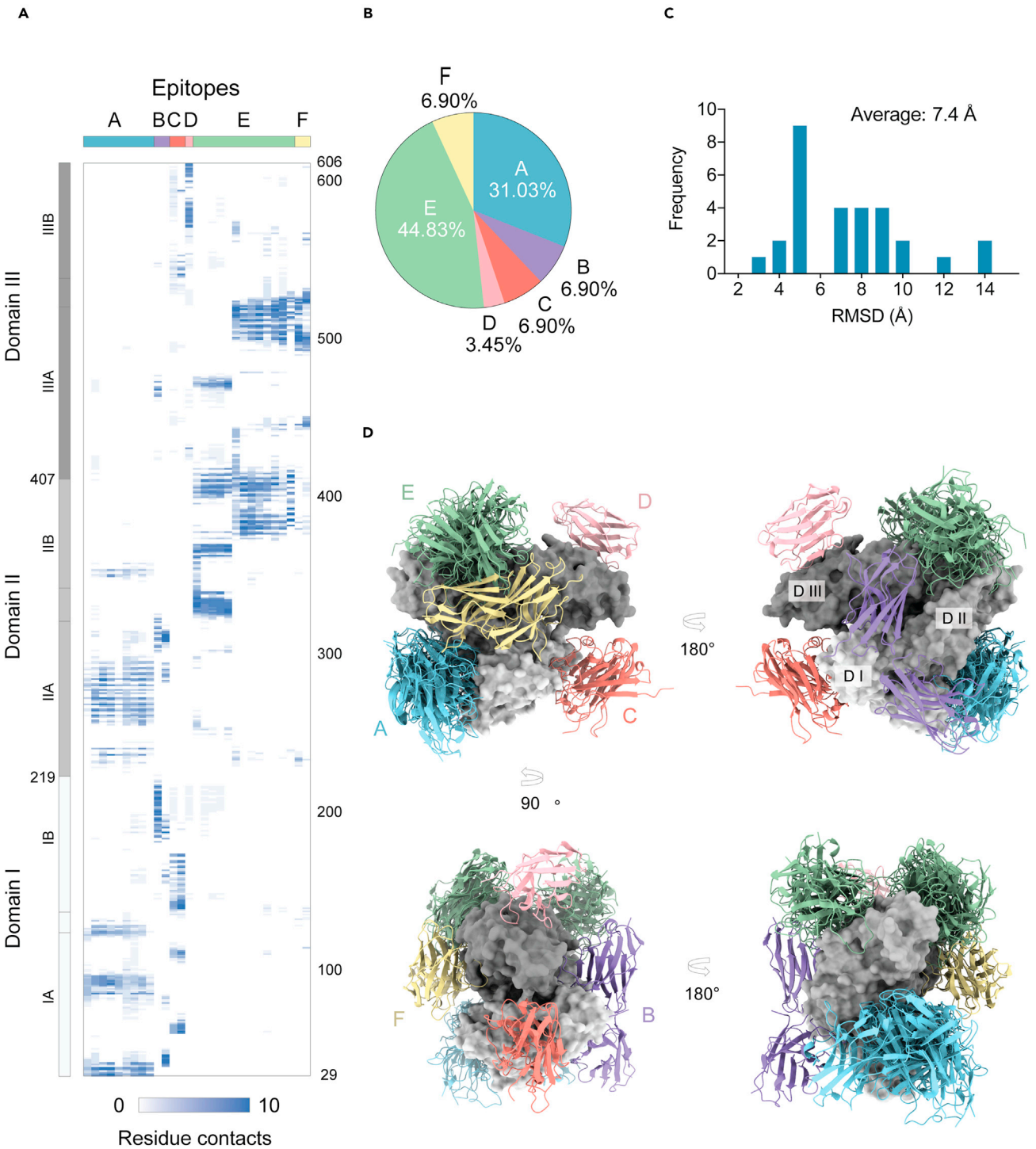


**Figure 2. Cross-link models of the HSA-Nb$_{HSA}$ complexes**

(A) The epitope clusters of HSA based on converged cross-link models. HSA Epitope cluster A: residues 29–37, 81–93, 118–124, 232, 236, 252–290, 300–310, 345–350; cluster B: residues 35–44, 179–212, 282–286, 298–318, 460–465; cluster C: residues 56–62, 101–108, 1234–169; cluster D: residues 426, 566–582, 595, 598–606; cluster F: 440–446, 488–525. Cluster E has two subtypes that share the same helices region and vary on other binding residues. E$_{type1}$: residues 321–331, 334–335, 358, 360–365, 395–413, 465–470; E$_{type2}$: residues 371–387, 396–410, 494–519.

(B) Percentage of epitope-specific Nb$_{HSA}$ based on converged cross-link models.

**Figure 2. *Continued***

(C) The RMSD (root-mean-square deviation, Å) distribution of the cross-link models.

(D) Integrative structural models of HSA-$Nb_{HSA}$ complexes. Only the top-scored $Nb_{HSA}$ models were shown. Different molecules were presented in different colors. Gray (surface presentation): HSA (with three domains DI, DII, and DIII). $Nb_{HSA}$ corresponding to different epitopes were presented as cartoons. Epitope Cluster (A): blue; (B): purple; (C): salmon; (D): light pink; (E): green; (F): yellow.

## Hybrid structural determination of a tetrameric HSA-Nb complex

Next, we used size-exclusion chromatography (SEC) to verify our structural proteomic results. Three Nbs ($Nb_{13}$, $Nb_{29}$, and $Nb_{80}$) which bind distinct epitopes (A, C, and E, respectively) were reconstituted in complex with HSA. The resulting complexes (HSA-$Nb_{80}$, HSA-$Nb_{80}$-$Nb_{29}$, and HSA-$Nb_{80}$-$Nb_{29}$-$Nb_{13}$) of different molecular weights were subsequently analyzed by SEC. As shown in Figure 3A, our analysis reveals that these Nbs do not compete with each other for HSA binding and do not share overlapping epitopes, which is consistent with epitope mapping by structural proteomics.

To obtain detailed structural information of Nb binding, we collected a homogenous fraction of the tetrameric complex composed of HSA and three Nbs for negative stain electron microscopy (EM) analysis. ~22,000 EM particles were subsequently selected to reconstruct the 3D density map (Figure S4, STAR methods). The EM map fits well the cross-linking model (Figure 3B). Moreover, compared to $Nb_{29}$ of relatively lower affinity ($K_D$ = 1.2 nM), we found that ultrahigh-affinity Nbs of $Nb_{80}$ ($K_D$ = 166 pM) and $Nb_{13}$ ($K_D$ = 201 pM) bind more concave epitopes (Figures 3C–3E). To further validate this integrative structure, we performed site-directed mutagenesis followed by immunoprecipitation to evaluate the binding of $Nb_{80}$ to two critical HSA residues (K383 and E400). Our model predicts that these residues form salt bridges with the CDR residues of $Nb_{80}$ (K383-D60 and E400-R107, Figure 3F). Therefore, simple charge reversals should disrupt the covalent bonds to reduce the ultrahigh-affinity of $Nb_{80}$ for HSA binding. Consistent with this model, we found that a single-point mutation E400R can substantially weaken $Nb_{80}$ binding. The binding was largely abolished by the double-residue mutations (K383D;E400R) that reversed two critical charges (Figure 3G).

## Paralleled Nb pharmacokinetic analysis by quantitative proteomics

ELISA has been extensively used to quantify the pharmacokinetics of biologics. This method requires the use of mAbs for specific, accurate, and reproducible quantifications of low-abundance signals in the complex serum background. However, high-quality mAbs are often difficult to obtain and may have large batch-to-batch variations (Baker, 2015; Sakamoto et al., 2018; Weller, 2016). The challenges are exacerbated for high-throughout pharmacokinetic analysis, which requires the use of a large number of laboratory animals (minimally, three animals per molecule such as Nb). The experiments can be highly laborious. To alleviate these potential issues and to minimize experimental biases, we developed a specific, sensitive, and paralleled pharmacokinetic assay based on parallel reaction monitoring or PRM mass spectrometry (MS) (Gallien et al., 2012; Peterson et al., 2012). For proof-of-concept, we chose four benchmark Nbs for assay development. Purified Nbs were spiked in the llama serum. The protein mixtures were then efficiently proteolyzed in solution by endoproteases such as trypsin to generate distinct Nb peptides that represent Nb signals. Desalted peptides were subsequently analyzed by LC coupled to label-free MS. The unique peptides and their specific fragment ions were selected for quantification by a high-resolution Orbitrap mass analyzer. Our analysis shows that the assay is sensitive and accurate. Less than 3 nM of Nbs in the llama serum can be detected with excellent quantification linearity ($R^2$ = 0.999) (Figure S5; Data S4).

To facilitate the pharmacokinetic analysis of $Nb_{HSA}$ (most do not bind mouse albumin), we used a humanized mouse model (B6.Cg-Tg(FCGRT)32Dcr *Alb*$^{em12Mvw}$ *Fcgrt*$^{tm1Dcr}$/MvwJ) (Roopenian et al., 2015) to approximate the half-life and physiology of HSA in humans. In this model, mouse *Alb* is removed, and *Fcgrt* is replaced with a human ortholog. HSA can be later administered in this model to study the pharmacokinetics of HSA-based drugs. These transgenic animals are healthy and fertile, consistent with the previous observations (Low and Wiles, 2016; Roopenian et al., 2015).

Following the HSA injection, 22 Nbs were mixed with equal molarity in PBS and were administered to the animals (n = 3) *via* single-bolus intravenous (*i.v.*) injections (STAR methods). This mixture includes 20 well-characterized and highly diverse $Nb_{HSA}$s and two control Nbs that do not bind HSA. These $Nb_{HSA}$s can bind albumin at the mildly acidic pH and span a wide range of binding affinities. Analysis of these Nbs may help better understand the contribution of binding at the endosomal pH to their *in vivo* pharmacokinetic

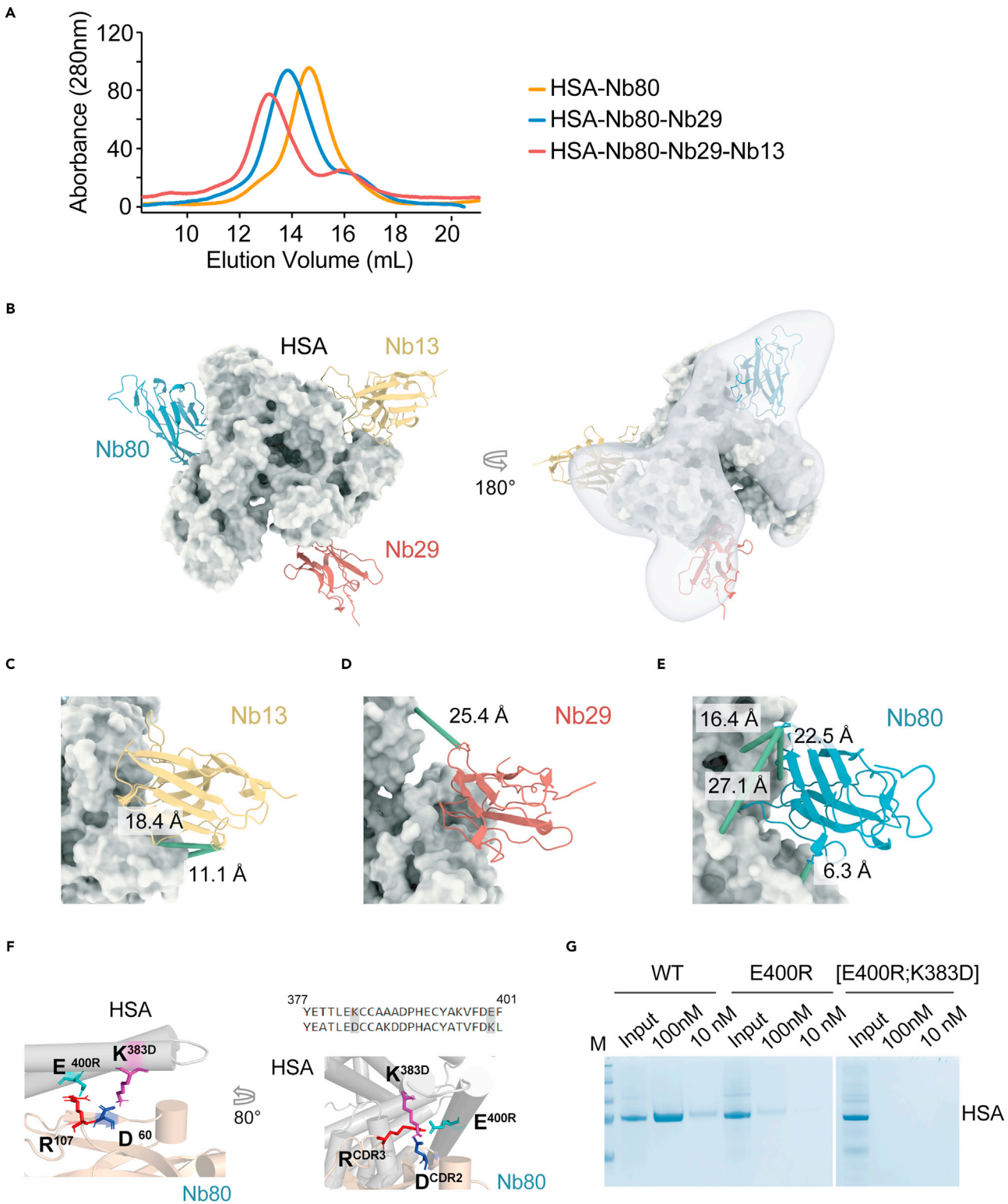


**Figure 3. Integrative structural characterization of a tetrameric HSA-Nb complex**

(A) Size-exclusion chromatography (SEC) analysis of the reconstituted tetrameric complex, including $Nb_{13}$, $Nb_{29}$, $Nb_{80}$, and HSA.

(B) Overlapping of the cross-link structure model of the tetrameric complex with the negative stain EM structure. $Nb_{HSA}$ were presented in different colors. Yellow: $Nb_{13}$; salmon: $Nb_{29}$; blue: $Nb_{80}$.

**Figure 3. *Continued***

(C–E) Close-up views of the interfaces of the tetrameric HSA-Nb complex and the cross-link restraints.

(F) A cross-link model of HSA and $Nb_{80}$ interaction showing the putative salt bridges. Sidechains of two charged residues on HSA (K383 and E400) and the corresponding residues on $Nb_{80}$ were shown. The HSA sequence (from residue 377 to residue 401) was aligned with camelid albumin.

(G) HSA site-directed mutagenesis and immunoprecipitation of the mutant HSA. $Nb_{80}$-conjugated resins were used to pull down different HSA mutants, including E400R and E400R-K383D.

properties (van Faassen et al., 2020). The molar ratio between Nbs and HSA was 1:5 to limit potential competitions among Nbs that target the same epitopes. Blood was collected at 17 different time points ranging from predose to 21 days postinjection (STAR methods). Serum samples were efficiently proteolyzed, and the diagnostic $Nb_{HSA}$ peptides and the fragment ions were accurately quantified as described above (Figure 4A; Data S4). The quantifications were highly reproducible and the median coefficient of variation (CV) of three biological replicates was 15.3% (Figure S6).

To measure pharmacokinetics, the average relative abundance of Nbs was calculated and fitted into a two-phase decay model to derive the half-lives (STAR methods). Our results reveal that control Nbs were rapidly cleared from the serum, with the half-lives of approximately 26–60 min, which are consistent with the previous ELISA measurements (Hoefman et al., 2015). In comparison, $Nb_{HSA}$s were substantially more stable in the serum. $Nb_{HSA}$s are generally characterized by fast distribution rates followed by slow elimination rates. However, each $Nb_{HSA}$ has a unique pharmacokinetic profile. The distribution half-lives span between 1.0 h ($Nb_{80}$) and 30.5 h ($Nb_{85}$). The elimination half-lives range from 1.6 days ($Nb_{100}$) to 7.6 days ($Nb_{75}$), which correspond to approximately 771-fold improvement compared to the control Nb (Figures 4B and 4C; Data S2). The half-lives of $Nb_{HSA}$s agree well with the relatively short half-life of HSA (~8 days) that we determined in this model (Figure S7C). Nevertheless, we expect that their pharmacokinetics will be substantially improved when applied to humans.

Serum proteomes contain rich molecular information regarding clinical manifestations and drug treatment (Durrum et al., 1956). To explore the potential serum proteomic alterations post-HSA administration and to understand the relatively fast half-life of HSA in this mouse model (8 days versus ~3 weeks in humans), we quantified the longitudinal blood proteomes by label-free quantitative proteomics (Anderson, 2010; Geyer et al., 2017).

A total of 441 blood proteins were quantified by MS for 10 days post-HSA administration. The quantified proteins were then clustered based on their relative abundance changes to generate the heatmap (Figure S8). Our analysis revealed a group of acute-phase inflammatory proteins, such as serum amyloid A and C-reactive protein, were drastically increased by hundreds of folds in 12–24 h postinjection, before returning to the baseline levels in 24–48 h (Sproston and Ashworth, 2018; Uhlar and Whitehead, 1999). This observation may be related to the acute response to *i.v.* injection and frequent blood sampling within the first 24 h or potential inflammations caused by administration of a large quantity of exogenous protein (HSA). In addition, we detected an increase of serum IgGs 5–7 days postadministration, which indicates a potential antibody response against the exogenous HSA and may explain the faster-than-expected clearance of HSA in this model (Schmidt et al., 2013). Further studies will be needed to evaluate these changes during Nb treatment.

## $Nb_{HSA}$ pharmacokinetics is related to the physicochemical and structural properties

To understand the diverse pharmacokinetics of $Nb_{HSA}$s better, we calculated the correlations of half-lives (including both elimination and distribution rates) with different biophysical and physicochemical properties such as HSA binding (at both neutral and mildly acidic pH), melting temperature ($T_M$), pI, and hydrophobicity. The resulting heatmaps were shown in Figure 4D. We found that 1) elimination and distribution rates of Nbs are positively correlated ($p = 0.018$), 2) compared to low/mediocre-affinity Nbs, high-affinity Nbs (sub-nM) have slower clearance rates, 3) the elimination half-lives of Nbs are positively correlated with binding affinities (ELISA O.D.) at the endosomal pH ($p = 0.003$), and 4) elimination seems to be positively correlated with the binding off-rates at neutral pH ($p = 0.006$), which may contribute to high-affinity binding at low pH. However, we did not observe any significant correlation between the elimination and binding affinity at neutral pH when both on- and off-rates are considered. Conceivably, both slow off-rates and binding at the mildly acidic pH are required to enable stable complex formation of the low-abundance, intracellular $Nb_{HSA}$-HSA-FcRn complex. $Nb_{HSA}$ that do not bind strongly to the complex have reduced *in vivo* half-life. In addition, Nb structures and epitopes may also contribute to the half-lives. For example, an ultrahigh-affinity

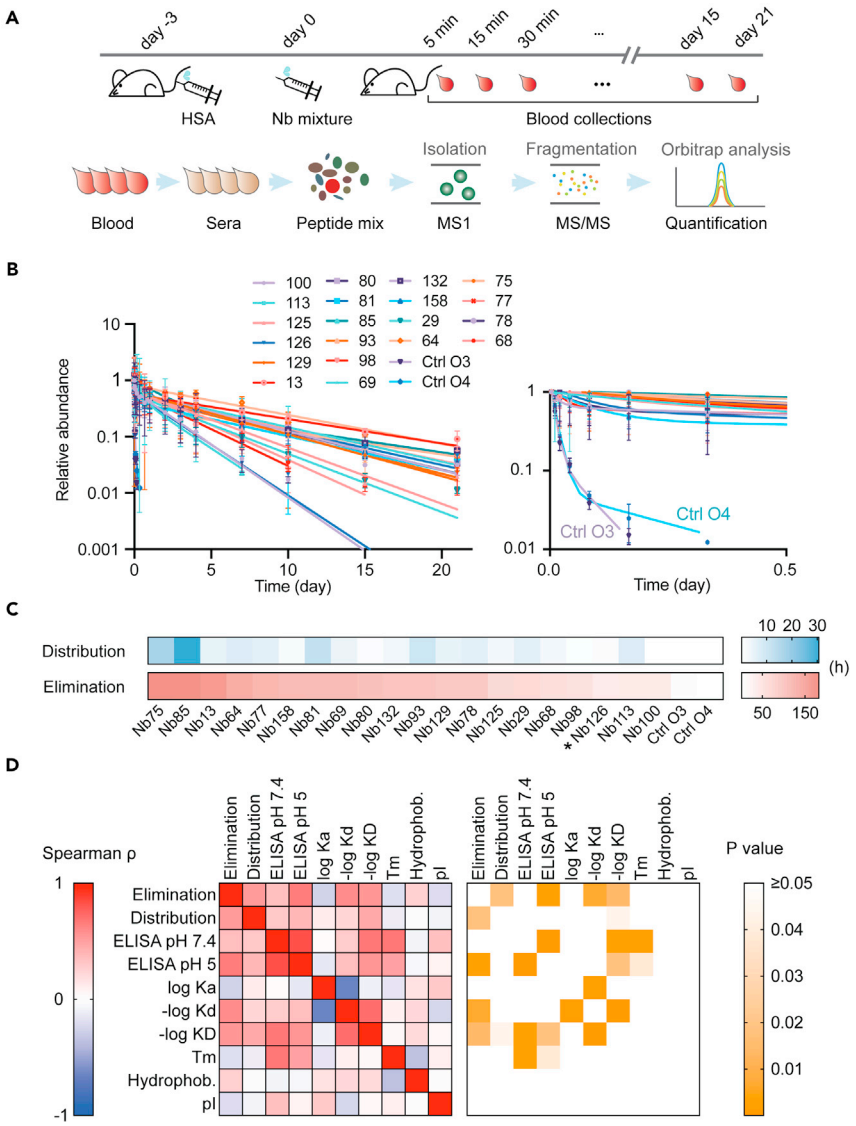


**Figure 4. High-throughput Nb pharmacokinetics in an Alb$^{-/-}$ FcRn-humanized mouse model**

(A) Schematics of the MS-based assay for multiplexed pharmacokinetic analysis. Briefly, after consecutive injections of HSA and the Nb mixtures into the mouse model, blood was collected at 21 different time points and processed for proteomics-based pharmacokinetic analysis.

(B) Pharmacokinetic analysis of 22 Nbs in an Alb$^{-/-}$ FcRn-humanized mouse model. Single bolus administration of an equimolar mixture of 22 Nbs, including 20 $Nb_{HSA}$ and two nonbinder controls were administered to three animals via *i.v.* injection. Serum samples were collected at different time points and proteolyzed. The resulting peptides were analyzed by LC coupled to MS (PRM). Each data point indicates the median Nb abundance from three different animals. The analysis was repeated three times. The data were then fitted into a two-phase decay model to calculate the Nb half-lives.

(C) Heatmap analysis of the distribution and elimination of Nb pharmacokinetics. *, See Figure S3A.

(D) Correlative analysis between pharmacokinetics and the properties of Nbs. For each correlation analysis, the correlation coefficient Spearman ρ, and the corresponding p-value were calculated using Prism GraphPad.

$Nb_{126}$, which is based on our structural model may interfere with the HSA-FcRn interaction, is characterized by fast elimination half-life (41.4 h) (Figure S3A) (Sand et al., 2015; Schmidt et al., 2013).

## Development of Nb-cytokine fusion constructs "Duraleukin" for cancer immunotherapy

Interleukin-2 (IL-2) is a cytokine that can modulate immune cells such as T cells and natural killer cells to inhibit tumor growth (Boyman and Sprent, 2012). Human IL-2 (hIL-2) is the first FDA-approved cancer

immunotherapy drug to treat renal cell carcinoma and metastatic melanoma (Rosenberg, 2014). High-dose hIL-2 (proleukin) is effective against these devastating cancers, and ~10% of patients who receive the treatment can expect a complete response. However, clinical efficacy of this cytokine-based immunotherapy is substantially limited by the small size (~15 kDa) and the poor pharmacokinetics of hIL-2 (elimination half-life of 85 min in humans) (Boyman and Sprent, 2012; Rosenberg, 2014). High-dose and repetitive administration (every 8 h), which are necessary for the sustained antitumor activity and clinical efficacy, can lead to severe side effects such as vascular leak syndrome and liver toxicity (Rosenberg, 2014; Schwartz et al., 2002).

Here, we developed Nb-fusion constructs to improve the antitumor efficacy of hIL-2 while potentially reducing the clinical side effects associated with high dose. Specifically, we generated constructs by genetically fusing several cross-species albumin Nbs ($Nb_{77}$, $Nb_{80}$, or $Nb_{158}$) N-terminal to hIL-2 (Figure 5A). A short flexible GS linker was inserted between IL-2 and the Nb. Based on structural models, this design will ensure that 1) the N-terminal fusion Nb does not sterically interfere with the hIL-2 binding to its receptor IL-2R and 2) hIL-2 does not block Nb binding to the FcRn receptor (Figure S9A). The resulting constructs "Duraleukins" were purified for *in vitro* and *in vivo* evaluations.

As shown in Figure 5B, we developed a protocol to isolate Duraleukin ($DL_{77}$, $DL_{80}$, and $DL_{158}$) from *E. coli* inclusion bodies (STAR methods). Recombinantly purified DLs demonstrated excellent thermostability ($T_m \approx 60°C$, Figure 5C) and remained highly stable when incubating at 37°C for days with fresh mouse sera that contain protease activities (Figure 5E). Critically, DLs had comparably high bioactivities to hIL-2 *in vitro* in stimulating the proliferation of $CD8^+$ T cells, as shown by the T cell proliferation assay (STAR methods; Figure 5D). Moreover, DLs retained ultrahigh HSA binding affinities (Figure 5E). Our results demonstrated the robust physicochemical properties and high bioactivities of Duraleukin. $DL_{80}$ was used for preclinical evaluations in an animal model. While the selection was primarily based on its fast distribution rate, high affinity, and partial resistance to acidic pH (Figure 5G), other DLs also have excellent stability and bioactivities that may translate into high preclinical efficacy as well.

### High preclinical efficacy of Duraleukin for melanoma treatment

To evaluate the preclinical efficacy of Duraleukin for cancer treatment, we generated a B16-F10 melanoma mouse model in the C57BL/6J background (Overwijk and Restifo, 2001). First, we confirmed the prolonged half-life of $DL_{80}$ (~46-fold improvement compared to hIL-2) in this model (Figure S9B). Next, tumor-bearing mice were randomly grouped into three arms and were intraperitoneally administered with $DL_{80}$, hIL-2, or PBS control for 24 days. The hIL-2 treated mice were dosed daily to counteract the limited bioactivity imposed by the short half-life of hIL-2. In comparison, the $DL_{80}$-treated arm was dosed every six days to evaluate the impact of half-life extension. In addition, a monoclonal antibody, TA99 was cotreated with both therapeutic agents. TA99 recognizes a melanoma surface marker TRP1 and has been shown to synergize with hIL-2 for improved anticancer activity in the mouse model (Moynihan et al., 2016; Silva et al., 2019; Sun et al., 2019; Zhu et al., 2015) (STAR methods). The tumor sizes and the survival of the treated animals were continuously monitored for up to 62 days before termination of the project (Figures 6A and 6B). Compared to the PBS control animals, both $DL_{80}$- and hIL-2-treated animals showed substantial reductions in tumor loads and significantly improved survival rates. In addition, we found that animals responding to $DL_{80}$ were almost entirely free of tumors, whereas rebounds of tumorigenesis in the hIL-2 treated mice were evident. Here, despite the low administration frequency and dose (as little as 13% of the hIL-2 dose), the high *in vivo* stability and sustainable anticancer activity of $DL_{80}$ may ultimately lead to the improved recovery of the treated animals.

To explore the mechanisms that underlie Duraleukin's high preclinical efficacy, we isolated the tumors three days post-treatment, sorted, and analyzed tumor-infiltrating immune cells by flow cytometry (Figures 6C and S10). We observed significant and more persistent increases of tumor-infiltrating immune cells, including both $CD8^+$ T cells and natural killer cells in the $DL_{80}$-treated tumor tissues compared to controls. Collectively, these results suggest that Duraleukin can consistently promote tumor-infiltrating immune cells to obtain highly sustainable antitumor activities.

## DISCUSSION

In this study, we have characterized a large collection of high-quality HSA Nbs for drug delivery. Using multidisciplinary approaches that span biophysics, structural proteomics, and modeling, we systematically mapped HSA epitopes and resolved the structure of a tetrameric HSA-Nb complex. Our analysis reveals that most of

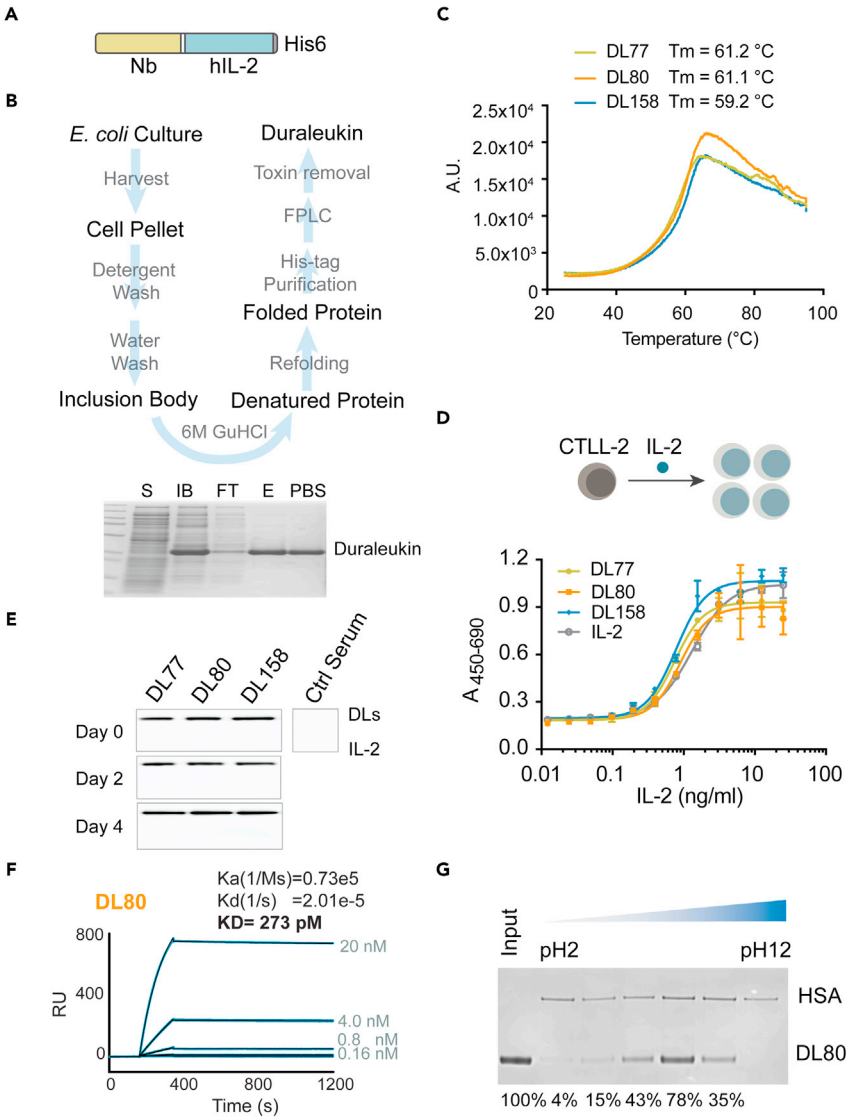


**Figure 5. Development of Duraleukin – a novel class of $Nb_{HSA}$-fusion cytokine**

(A) Schematic design of Duraleukin, including an N-terminal $Nb_{HSA}$, a short flexible linker sequence ($(GGGGS)_2$), and hIL-2 followed by a C-terminal His6 tag.

(B) Schematics of large-scale Duraleukin production from *E. coli*. A representative SDS-PAGE analysis of purified Duraleukin. S: soluble fraction. IB: inclusion body; FT: flow-through; E: elution; PBS: after endotoxin removal and dialysis in PBS.

(C) Thermostability of Duraleukins by differential scanning fluorimetry.

(D) *In vitro* CTLL-2 cell proliferation assay of Duraleukin and hIL-2. The X axis is the concentration of hIL-2 (ng/mL). The Y axis is the absorbance at 450 nM subtracted by absorbance at 690 nm (background signal) for the measurement of T cell proliferation.

(E) The resistance of three DLs to serum proteases. Purified DLs were incubated with the mouse serum for the indicated periods. After incubation, DLs were detected by western blot using an anti-IL-2 monoclonal antibody (BG5).

(F) The SPR kinetic measurement of $DL_{80}$ for HSA binding.

(G) Immunoprecipitation assay (pH-dependent) of $DL_{80}$ for HSA binding. HSA-conjugated agarose resin was used to pull down $DL_{80}$ at various concentrations. Immunoprecipitated $DL_{80}$ at different pH was normalized and quantified by ImageJ.

Nbs bind to HSA at sub-nanomolar affinities, which are unusual for single-domain antibody fragments (Xiang et al., 2021). Several Nbs also bind strongly with monkey and mouse albumins which could be useful for efficacy studies in these preclinical models. Moreover, our systematic structural investigations have identified multiple Nb epitope classes on HSA. This information has provided a structural basis to better understand Nb binding and may help future design of novel therapeutics to target HSA as an important drug target.

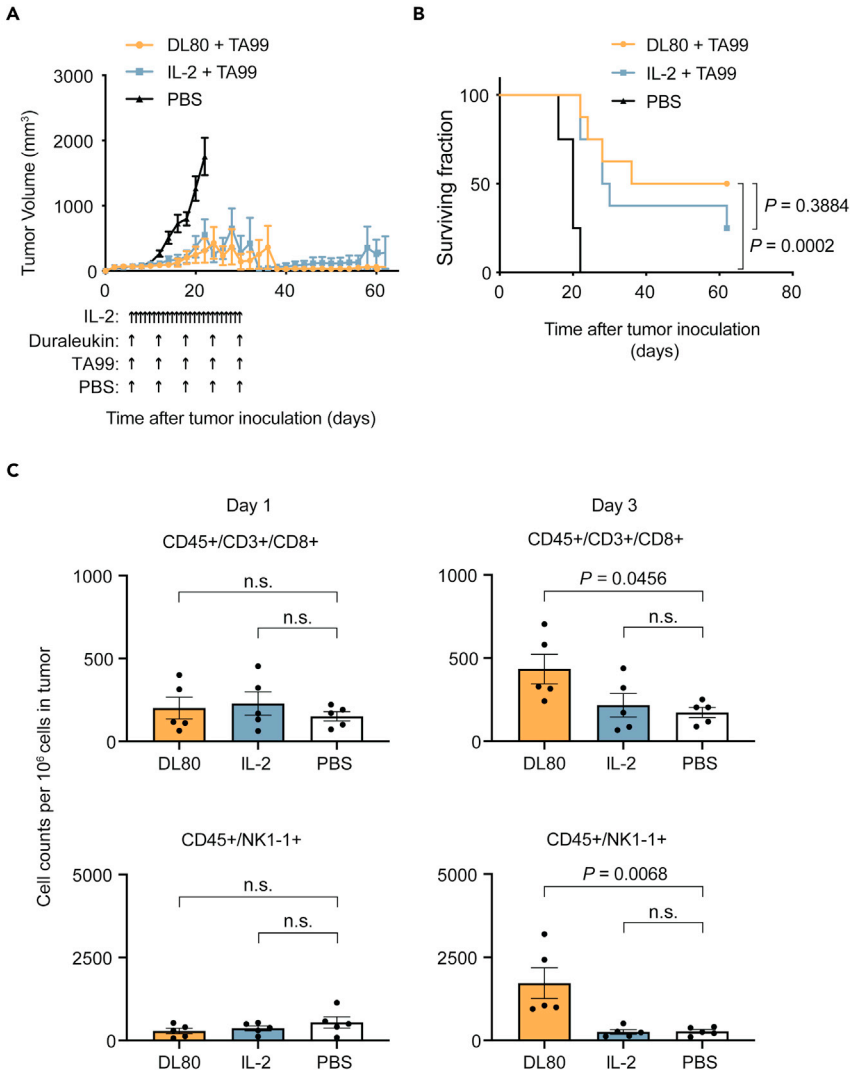


**Figure 6. Evaluation of the *in vivo* efficacy of Duraleukin in a melanoma mouse model**

(A) The tumor growth curve. C57BL/6J mice bearing subcutaneous B16-F10 tumors were treated with a combination of TA99 and Duraleukin or hIL-2 (n = 8/group) with different dosage intervals. PBS treatment was used for control.

(B) Animal survival curve after treatment.

(C) Flow cytometry analysis of tumor-infiltrating immune cells (n = 5/group). The y axis is the respective immune cell count based on a million total cells from the isolated tumor.

We have developed a sensitive and quantitative MS-based protocol for paralleled analysis of Nb pharmacokinetics. Using an HSA transgenic mouse model, we have determined the pharmacokinetics of dozens of Nbs. $Nb_{HSA}$s are characterized with distinct and highly extended half-lives, which correlate with the binding affinity at the endosomal pH. Our data indicate that high-affinity albumin binding is critical for the half-lives of $Nb_{HSA}$s (Merlot et al., 2014; Peters, 1996; Pyzik et al., 2015). These $Nb_{HSA}$s may have substantially improved half-lives in humans.

Previous studies have reported the use of albumin Nbs for drug delivery. However, these Nbs have not been systematically characterized with few sequences publicly available (Chen et al., 2021; Coppieters et al., 2006; Fleming et al., 2020; Fuchs and Igney, 2017; Hoefman et al., 2015; Müller et al., 2012; Steeland et al., 2015; Terryn et al., 2014; Tijink et al., 2008; Vosjan et al., 2012). Most recently, van Faassen et al. developed several high-quality $Nb_{HSA}$s with nanomolar affinities (van Faassen et al., 2020). Domain mapping and alanine scanning help to locate the binding region of Nbs. In this study, they also evaluated Nb binding to

the FcRn-HSA complex *in vitro* at different pH and demonstrated the extended half-lives of their $Nb_{HSA}$s and the fusion constructs *in vivo*. Together, these studies greatly expanded the diversity of drug-quality albumin Nbs, providing a repertoire of Nbs with high flexibility to potentially modify drug half-life based on specific clinical requirements.

High-quality $Nb_{HSA}$s may offer several major advantages over the Fc-based methods for drug delivery. Firstly, compared to Fc (~50 kDa), Nbs are substantially smaller (~15 kDa). Therefore, Nb-fusion constructs have higher molar concentrations per administration (and effective therapeutic dose) than the Fc-fusion counterparts. Secondly, Nbs have a robust fold to facilitate bioengineering and retain the bioactivities of the modified targets (Larsen et al., 2016; Sleep et al., 2013). Affinity-matured Nbs are characterized by high stability that allows for direct inhalation therapy by Nb aerosols for the treatment of pulmonary infections highly efficiently (Larios Mora et al., 2018; Liang et al., 2020; Nambulli et al., 2021; Patton and Byron, 2007). Their marked physiochemical properties will also be critical for drug storage, administration, and delivery (Holliger and Hudson, 2005). Finally, Nbs do not recruit functional immune cells as the Fc domain of antibody does. While this may not be ideal for applications in which the Fc-mediated effector's functions are required, it will be useful when elevated immune responses (e.g., against the IL-$2R^+$ cells) should be minimized (Hassanzadeh-Ghassabeh et al., 2013; Kang and Jung, 2019; Steeland et al., 2016). In addition, for the neutralization of viruses, Fc has been associated with antibody-dependent enhancement (ADE) which may increase the risk of exacerbating disease severity (Katzelnick et al., 2017; Polack et al., 2003). In these cases, it might be necessary to mutate Fc to abolish its associated immune responses.

To demonstrate the utility of this resource, we have generated IL-2-fusion constructs (Duraleukin) using high-quality, cross-species $Nb_{HSA}$s that help translate the preclinical results into clinical trials. Critically, despite using a substantially lower administration dose, Duraleukin outperformed hIL-2 for melanoma treatment. The improved efficacy is likely the results of enhanced half-life of $Nb_{HSA}$-modified hIL-2 and the accumulation of tumor-infiltrating immune cells. Presumably, it is also related to the high local concentration of albumin in the tumor interstitium and high bioactivity of Duraleukin in the tumor tissue (Finicle et al., 2018; Greish, 2007; Merlot et al., 2014).

This proof-of-concept study is readily extended to other small antitumor cytokines (Steel et al., 2012), ultimately leading to enhanced antitumor activity, low-dosing regimen, and improved safety profiles for human applications. It is conceivable that a combination of Duraleukin and an immune checkpoint blockade therapy like PD-1/L1 or CTLA-4 may further synergistically improve cancer treatment (Khair et al., 2019; Ring et al., 2013). It is also feasible to quickly generate a trifunctional construct by fusing Duraleukin with another Nb that specifically recognizes a tumor surface marker such as EGFR or HER2 for a more target-specific therapy (Hirsch et al., 2009). Future studies will be needed to investigate $Nb_{HSA}$ and Duraleukin in the preclinical and clinical settings.

### Limitations of the study

In this study, we have determined the pharmacokinetics of highly selected albumin Nbs in an $Alb^{-/-}$ FcRn-humanized mouse model. In this model, we found that the half-lives of $Nb_{HSA}$s are drastically improved compared to control Nbs. However, these transgenic animals may or may not fully recapitulate the physiology of albumin and its transcytosis biology in humans. Further investigations in NHPs and preferentially humans would help more accurate determination of the half-lives of our $Nb_{HSA}$s for clinical development.

Moreover, in the current study, we did not investigate the optimal dosing of Duraleukin for tumor growth inhibition. It would also be interesting to assess the efficacy of Duraleukin in renal cell carcinoma models.

## STAR★METHODS

Detailed methods are provided in the online version of this paper and include the following:

- KEY RESOURCES TABLE
- RESOURCE AVAILABILITY
  - Lead contact
  - Materials availability
  - Data and code availability
- EXPERIMENTAL MODEL AND SUBJECT DETAILS

- Animals
- Cell lines
- METHOD DETAILS
  - Nb DNA synthesis and cloning
  - Nb purification
  - ELISA (enzyme-linked immunosorbent assay)
  - *In vitro* pull-down assay (immunoprecipitation)
  - Nb affinity measurement by surface plasmon resonance (SPR)
  - Clustering and phylogenetic tree analysis of $Nb_{HSA}$
  - Thermostability analysis of $Nb_{HSA}$
  - Chemical cross-linking and mass spectrometry (CXMS)
  - Integrative structural modeling of HSA-Nb complexes
  - Size-exclusion chromatography (SEC) and negative stain electron microscopy
  - Site-directed mutagenesis
  - MS quantification of Nb pharmacokinetics
  - Serum proteomic quantification
  - Purification of duraleukins
  - *In vitro* T cell proliferation assay
  - Generation and treatment of melanoma mouse model
  - Flow cytometry
- QUANTIFICATION AND STATISTICAL ANALYSIS

## SUPPLEMENTAL INFORMATION

Supplemental information can be found online at https://doi.org/10.1016/j.isci.2021.103014.

## ACKNOWLEDGMENTS

This work was supported by University of Pittsburgh Medical Center Aging Institute pilot fund (Y.S.), National Institutes of Health grants 1R35GM137905 (Y.S.), R01-GM097082 (C.J.C. and U.S.), R01HL137709 (K.C.), and Israeli Science Foundation 1466/18, Israel Ministry of Science and Technology (D.S.).

## AUTHOR CONTRIBUTIONS

Y.S and Z. Shen conceived the research. Y.S. supervised the studies. Y.X and Y.S identified the Nbs. Z. Shen and Y.X performed major experiments and data analysis with help from Y.S, S.V, Z.X, A.V, C.J, G.C, B.H, G.C, Z. Sang, J.L, and K.C. D.S and C.C performed structural modeling. Thank P.W. Duprex (Vaccine center, Pitt) for his assistance in the SPR experiments, D.Goebe, for the critical reading of the manuscript. Y.S and Z.S drafted the manuscript with input from all the authors.

## DECLARATION OF INTERESTS

University of Pittsburgh has filed a provisional patent in which Z.S and Y.S are listed as co-inventors. The Duraleukin technology is licensed to a university start-up Antenna Biotechnology Inc. (founded by Y.S).

Received: February 16, 2021
Revised: June 9, 2021
Accepted: August 18, 2021
Published: September 24, 2021

## REFERENCES

Anderson, N.L. (2010). The clinical plasma proteome: a survey of clinical assays for proteins in plasma and serum. Clin. Chem. *56*, 177–185.

Baker, M. (2015). Reproducibility crisis: blame it on the antibodies. Nature *521*, 274–276.

Boyman, O., and Sprent, J. (2012). The role of interleukin-2 during homeostasis and activation of the immune system. Nat. Rev. Immunol. *12*, 180–190.

Carter, P.J. (2006). Potent antibody therapeutics by design. Nat. Rev. Immunol. *6*, 343–357.

Chait, B.T., Cadene, M., Olinares, P.D., Rout, M.P., and Shi, Y. (2016). Revealing higher order protein structure using mass spectrometry. J. Am. Soc. Mass Spectrom. *27*, 952–965.

Chen, X., Bian, Y., Xie, Y., Zheng, N., Nie, K., Liu, R., Yan, M., Luo, H., Wang, H., Yang, J., et al. (2021). A dual target-directed single domain-based fusion protein against interleukin-6 receptor decelerate experimental arthritis progression via modulating JNK expression. Inflammation *44*, 1620–1628.

Chen, Z.-L., Meng, J.-M., Cao, Y., Yin, J.-L., Fang, R.-Q., Fan, S.-B., Liu, C., Zeng, W.-F., Ding, Y.-H., Tan, D., et al. (2019). A high-speed search engine pLink 2 with systematic evaluation for proteome-scale identification of cross-linked peptides. Nat. Commun. *10*, 3404.

Coppieters, K., Dreier, T., Silence, K., de Haard, H., Lauwereys, M., Casteels, P., Beirnaert, E., Jonckheere, H., Van de Wiele, C., Staelens, L., et al. (2006). Formatted anti-tumor necrosis factor alpha VHH proteins derived from camelids show superior potency and targeting to inflamed joints in a murine model of collagen-induced arthritis. Arthritis Rheum. *54*, 1856–1866.

Cox, J., and Mann, M. (2008). MaxQuant enables high peptide identification rates, individualized p.p.b.-range mass accuracies and proteome-wide protein quantification. Nat. Biotechnol. *26*, 1367–1372.

Crooks, G.E., Hon, G., Chandonia, J.M., and Brenner, S.E. (2004). WebLogo: a sequence logo generator. Genome Res. *14*, 1188–1190.

Cunningham, S., Piedra, P.A., Martinon-Torres, F., Szymanski, H., Brackeva, B., Dombrecht, E., Detalle, L., and Fleurinck, C. (2021). Nebulised ALX-0171 for respiratory syncytial virus lower respiratory tract infection in hospitalised children: a double-blind, randomised, placebo-controlled, phase 2b trial. Lancet Respir. Med. *9*, 21–32.

Czajkowsky, D.M., Hu, J., Shao, Z., and Pleass, R.J. (2012). Fc-fusion proteins: new developments and future perspectives. EMBO Mol. Med. *4*, 1015–1028.

D Brooks, B. (2014). The importance of epitope binning for biological drug discovery. Curr. Drug Discov. Tech. *11*, 109–112.

Dong, G.Q., Fan, H., Schneidman-Duhovny, D., Webb, B., and Sali, A. (2013). Optimized atomic statistical potentials: assessment of protein interfaces and loops. Bioinformatics *29*, 3158–3166.

Durrum, E.L., Jencks, W.P., and Smith, E.R. (1956). The clinical significance of the analysis of serum protein distribution by filter paper electrophoresis. Am. J. Med. *21*, 387–405.

Fernandez-Martinez, J., Kim, S.J., Shi, Y., Upla, P., Pellarin, R., Gagnon, M., Chemmama, I.E., Wang, J., Nudelman, I., Zhang, W., et al. (2016). Structure and function of the nuclear pore complex cytoplasmic mRNA export platform. Cell *167*, 1215–1228.e25.

Finicle, B.T., Jayashankar, V., and Edinger, A.L. (2018). Nutrient scavenging in cancer. Nat. Rev. Cancer *18*, 619–633.

Fleming, B.D., Urban, D.J., Hall, M.D., Longerich, T., Greten, T.F., Pastan, I., and Ho, M. (2020). Engineered Anti-GPC3 Immunotoxin, HN3-ABD-T20, Produces regression in mouse liver cancer xenografts through prolonged serum retention. Hepatology *71*, 1696–1711.

Flyak, A.I., Kuzmina, N., Murin, C.D., Bryan, C., Davidson, E., Gilchuk, P., Gulka, C.P., Ilinykh, P.A., Shen, X., and Huang, K. (2018). Broadly neutralizing antibodies from human survivors target a conserved site in the Ebola virus glycoprotein HR2–MPER region. Nat. Microbiol. *3*, 670–677.

Fridy, P.C., Li, Y., Keegan, S., Thompson, M.K., Nudelman, I., Scheid, J.F., Oeffinger, M., Nussenzweig, M.C., Fenyö, D., Chait, B.T., et al. (2014). A robust pipeline for rapid production of versatile nanobody repertoires. Nat. Methods *11*, 1253–1260.

Fuchs, H., and Igney, F. (2017). Binding to ocular albumin as a half-life extension principle for intravitreally injected drugs: evidence from mechanistic rat and rabbit studies. J. Ocul. Pharmacol. Ther. *33*, 115–122.

Gallien, S., Duriez, E., Crone, C., Kellmann, M., Moehring, T., and Domon, B. (2012). Targeted proteomic quantification on quadrupole-orbitrap mass spectrometer. Mol. Cell Proteomics *11*, 1709–1723.

Geyer, P.E., Holdt, L.M., Teupser, D., and Mann, M. (2017). Revisiting biomarker discovery by plasma proteomics. Mol. Syst. Biol. *13*, 942.

Ghuman, J., Zunszain, P.A., Petitpas, I., Bhattacharya, A.A., Otagiri, M., and Curry, S. (2005). Structural basis of the drug-binding specificity of human serum albumin. J. Mol. Biol. *353*, 38–52.

Greish, K. (2007). Enhanced permeability and retention of macromolecular drugs in solid tumors: a royal gate for targeted anticancer nanomedicines. J. Drug Target *15*, 457–464.

Hamers-Casterman, C., Atarhouch, T., Muyldermans, S., Robinson, G., Hamers, C., Songa, E.B., Bendahman, N., and Hamers, R. (1993). Naturally occurring antibodies devoid of light chains. Nature *363*, 446–448.

Harmsen, M.M., and De Haard, H.J. (2007). Properties, production, and applications of camelid single-domain antibody fragments. Appl. Microbiol. Biotechnol. *77*, 13–22.

Harris, J.M., and Chess, R.B. (2003). Effect of pegylation on pharmaceuticals. Nat. Rev. Drug Discov. *2*, 214–221.

Hassanzadeh-Ghassabeh, G., Devoogdt, N., De Pauw, P., Vincke, C., and Muyldermans, S. (2013). Nanobodies and their potential applications. Nanomedicine *8*, 1013–1026.

Heinrich, L., Tissot, N., Hartmann, D.J., and Cohen, R. (2010). Comparison of the results obtained by ELISA and surface plasmon resonance for the determination of antibody affinity. J. Immunol. Methods *352*, 13–22.

Hirsch, F.R., Varella-Garcia, M., and Cappuzzo, F. (2009). Predictive value of EGFR and HER2 overexpression in advanced non-small-cell lung cancer. Oncogene *28* (*Suppl 1*), S32–S37.

Hoefman, S., Ottevaere, I., Baumeister, J., and Sargentini-Maier, M.L. (2015). Pre-clinical intravenous serum pharmacokinetics of albumin binding and non-half-life extended Nanobodies®. Antibodies *4*, 141–156.

Holliger, P., and Hudson, P.J. (2005). Engineered antibody fragments and the rise of single domains. Nat. Biotechnol. *23*, 1126–1136.

Jovčevska, I., and Muyldermans, S. (2020). The therapeutic potential of nanobodies. BioDrugs *34*, 11–26.

Kang, T.H., and Jung, S.T. (2019). Boosting therapeutic potency of antibodies by taming Fc domain functions. Exp. Mol. Med. *51*, 1–9.

Katzelnick, L.C., Gresh, L., Halloran, M.E., Mercado, J.C., Kuan, G., Gordon, A., Balmaseda, A., and Harris, E. (2017). Antibody-dependent enhancement of severe dengue disease in humans. Science *358*, 929–932.

Khair, D.O., Bax, H.J., Mele, S., Crescioli, S., Pellizzari, G., Khiabany, A., Nakamura, M., Harris, R.J., French, E., Hoffmann, R.M., et al. (2019). Combining immune checkpoint inhibitors: established and emerging targets and strategies to improve outcomes in melanoma. Front. Immunol. *10*, 453.

Kijanka, M., Dorresteijn, B., Oliveira, S., and van Bergen en Henegouwen, P.M.P. (2015). Nanobody-based cancer therapy of solid tumors. Nanomedicine (Lond) *10*, 161–174.

Kim, S.J., Fernandez-Martinez, J., Nudelman, I., Shi, Y., Zhang, W., Raveh, B., Herricks, T., Slaughter, B.D., Hogan, J.A., Upla, P., et al. (2018). Integrative structure and functional anatomy of a nuclear pore complex. Nature *555*, 475–482.

Kontermann, R.E. (2016). Half-life extended biotherapeutics. Expert Opin. Biol. Ther. *16*, 903–915.

Kratz, F. (2008). Albumin as a drug carrier: design of prodrugs, drug conjugates and nanoparticles. J. Control Release *132*, 171–183.

Larios Mora, A., Detalle, L., Gallup, J.M., Van Geelen, A., Stohr, T., Duprez, L., and Ackermann, M.R. (2018). Delivery of ALX-0171 by inhalation greatly reduces respiratory syncytial virus disease in newborn lambs. MAbs *10*, 778–795.

Larsen, M.T., Kuhlmann, M., Hvam, M.L., and Howard, K.A. (2016). Albumin-based drug delivery: harnessing nature to cure disease. Mol. Cell Ther. *4*, 3.

Letunic, I., and Bork, P. (2007). Interactive Tree of Life (iTOL): an online tool for phylogenetic tree display and annotation. Bioinformatics *23*, 127–128.

Liang, W., Pan, H.W., Vllasaliu, D., and Lam, J.K.W. (2020). Pulmonary delivery of biological drugs. Pharmaceutics *12*, 1025.

Low, B.E., and Wiles, M.V. (2016). A humanized mouse model to study human albumin and albumin conjugates pharmacokinetics. Methods Mol. Biol. *1438*, 115–122.

Mastronarde, D.N., and Held, S.R. (2017). Automated tilt series alignment and tomographic reconstruction in IMOD. J. Struct. Biol. *197*, 102–113.

Merlot, A.M., Kalinowski, D.S., and Richardson, D.R. (2014). Unraveling the mysteries of serum albumin-more than just a serum protein. Front. Physiol. *5*, 299.

Moynihan, K.D., Opel, C.F., Szeto, G.L., Tzeng, A., Zhu, E.F., Engreitz, J.M., Williams, R.T., Rakhra, K., Zhang, M.H., Rothschilds, A.M., et al. (2016). Eradication of large established tumors in mice by combination immunotherapy that engages innate and adaptive immune responses. Nat. Med. *22*, 1402–1410.

Müller, M.R., Saunders, K., Grace, C., Jin, M., Piche-Nicholas, N., Steven, J., O'Dwyer, R., Wu, L., Khetemenee, L., Vugmeyster, Y., et al. (2012). Improving the pharmacokinetic properties of biologics by fusion to an anti-HSA shark VNAR domain. MAbs *4*, 673–685.

Nambulli, S., Xiang, Y., Tilston-Lunel, N.L., Rennick, L.J., Sang, Z., Klimstra, W.B., Reed, D.S., Crossland, N.A., Shi, Y., and Duprex, W.P. (2021). Inhalable nanobody (PiN-21) prevents and treats SARS-CoV-2 infections in Syrian hamsters at ultra-low doses. Sci. Adv. *7*, eabh0319.

Niesen, F.H., Berglund, H., and Vedadi, M. (2007). The use of differential scanning fluorimetry to detect ligand interactions that promote protein stability. Nat. Protoc. *2*, 2212–2221.

Nivarthi, U.K., Kose, N., Sapparapu, G., Widman, D., Gallichotte, E., Pfaff, J.M., Doranz, B.J., Weiskopf, D., Sette, A., and Durbin, A.P. (2017). Mapping the human memory B cell and serum neutralizing antibody responses to dengue virus serotype 4 infection and vaccination. J. Virol. *91*, e02016–e02041.

Ovacik, M., and Lin, K. (2018). Tutorial on monoclonal antibody pharmacokinetics and its considerations in early development. Clin. Transl Sci. *11*, 540–552.

Overwijk, W.W., and Restifo, N.P. (2001). B16 as a mouse model for human melanoma. Curr. Protoc. Immunol., Chapter 20, Unit 20.21.

Patton, J.S., and Byron, P.R. (2007). Inhaling medicines: delivering drugs to the body through the lungs. Nat. Rev. Drug Discov. *6*, 67–74.

Peters, T. (1996). All about Albumin : Biochemistry, Genetics, and Medical Applications (Academic Press).

Peterson, A.C., Russell, J.D., Bailey, D.J., Westphall, M.S., and Coon, J.J. (2012). Parallel reaction monitoring for high resolution and high mass accuracy quantitative, targeted proteomics. Mol. Cell Proteomics *11*, 1475–1488.

Pettersen, E.F., Goddard, T.D., Huang, C.C., Couch, G.S., Greenblatt, D.M., Meng, E.C., and Ferrin, T.E. (2004). UCSF Chimera–a visualization system for exploratory research and analysis. J. Comput. Chem. *25*, 1605–1612.

Pettersen, E.F., Goddard, T.D., Huang, C.C., Meng, E.C., Couch, G.S., Croll, T.I., Morris, J.H., and Ferrin, T.E. (2021). UCSF ChimeraX: structure visualization for researchers, educators, and developers. Protein Sci. *30*, 70–82.

Pleiner, T., Bates, M., Trakhanov, S., Lee, C.-T., Schliep, J.E., Chug, H., Böhning, M., Stark, H., Urlaub, H., and Görlich, D. (2015). Nanobodies: site-specific labeling for super-resolution imaging, rapid epitope-mapping and native protein complex isolation. Elife *4*, e11349.

Polack, F.P., Hoffman, S.J., Crujeiras, G., and Griffin, D.E. (2003). A role for nonprotective complement-fixing antibodies with low avidity for measles virus in atypical measles. Nat. Med. *9*, 1209–1213.

Pyzik, M., Rath, T., Lencer, W.I., Baker, K., and Blumberg, R.S. (2015). FcRn: the architect behind the immune and nonimmune functions of IgG and albumin. J. Immunol. *194*, 4595–4603.

Ring, A.M., Manglik, A., Kruse, A.C., Enos, M.D., Weis, W.I., Garcia, K.C., and Kobilka, B.K. (2013). Adrenaline-activated structure of beta2-adrenoceptor stabilized by an engineered nanobody. Nature *502*, 575–579.

Roopenian, D.C., Low, B.E., Christianson, G.J., Proetzel, G., Sproule, T.J., and Wiles, M.V. (2015). Albumin-deficient mouse models for studying metabolism of human albumin and pharmacokinetics of albumin-based drugs. MAbs *7*, 344–351.

Rosenberg, S.A. (2014). IL-2: the first effective immunotherapy for human cancer. J. Immunol. *192*, 5451–5458.

Rout, M.P., and Sali, A. (2019). Principles for integrative structural biology studies. Cell *177*, 1384–1403.

Russel, D., Lasker, K., Webb, B., Velazquez-Muriel, J., Tjioe, E., Schneidman-Duhovny, D., Peterson, B., and Sali, A. (2012). Putting the pieces together: integrative modeling platform software for structure determination of macromolecular assemblies. PLoS Biol. *10*, e1001244.

Sakamoto, S., Putalun, W., Vimolmangkang, S., Phoolcharoen, W., Shoyama, Y., Tanaka, H., and Morimoto, S. (2018). Enzyme-linked immunosorbent assay for the quantitative/qualitative analysis of plant secondary metabolites. J. Nat. Med. *72*, 32–42.

Sand, K.M.K., Bern, M., Nilsen, J., Noordzij, H.T., Sandlie, I., and Andersen, J.T. (2015). Unraveling the interaction between FcRn and albumin: opportunities for design of albumin-based therapeutics. Front. Immunol. *5*, 1–21.

Scheres, S.H. (2012). RELION: implementation of a Bayesian approach to cryo-EM structure determination. J. Struct. Biol. *180*, 519–530.

Schmidt, M.M., Townson, S.A., Andreucci, A.J., King, B.M., Schirmer, E.B., Murillo, A.J., Dombrowski, C., Tisdale, A.W., Lowden, P.A., Masci, A.L., et al. (2013). Crystal structure of an HSA/FcRn complex reveals recycling by competitive mimicry of HSA ligands at a pH-dependent hydrophobic interface. Structure *21*, 1966–1978.

Schneidman-Duhovny, D., Inbar, Y., Nussinov, R., and Wolfson, H.J. (2005). PatchDock and SymmDock: servers for rigid and symmetric docking. Nucleic Acids Res. *33*, W363–W367.

Schneidman-Duhovny, D., and Wolfson, H.J. (2020). Modeling of multimolecular complexes. Methods Mol. Biol. *2112*, 163–174.

Schwartz, R.N., Stover, L., and Dutcher, J.P. (2002). Managing toxicities of high-dose interleukin-2. Oncology (Williston Park) *16*, 11–20.

Scully, M., Cataland, S.R., Peyvandi, F., Coppo, P., Knöbl, P., Kremer Hovinga, J.A., Metjian, A., de la Rubia, J., Pavenski, K., Callewaert, F., et al. (2019). Caplacizumab treatment for acquired thrombotic thrombocytopenic purpura. N. Engl. J. Med. *380*, 335–346.

Shi, Y., Fernandez-Martinez, J., Tjioe, E., Pellarin, R., Kim, S.J., Williams, R., Schneidman-Duhovny, D., Sali, A., Rout, M.P., and Chait, B.T. (2014). Structural characterization by cross-linking reveals the detailed architecture of a coatomer-related heptameric module from the nuclear pore complex. Mol. Cell Proteomics *13*, 2927–2943.

Shi, Y., Pellarin, R., Fridy, P.C., Fernandez-Martinez, J., Thompson, M.K., Li, Y., Wang, Q.J., Sali, A., Rout, M.P., and Chait, B.T. (2015). A strategy for dissecting the architectures of native macromolecular assemblies. Nat. Methods *12*, 1135–1138.

Sievers, F., and Higgins, D.G. (2014). Clustal Omega, accurate alignment of very large numbers of sequences. Methods Mol. Biol. *1079*, 105–116.

Silva, D.A., Yu, S., Ulge, U.Y., Spangler, J.B., Jude, K.M., Labão-Almeida, C., Ali, L.R., Quijano-Rubio, A., Ruterbusch, M., Leung, I., et al. (2019). De novo design of potent and selective mimics of IL-2 and IL-15. Nature *565*, 186–191.

Sleep, D., Cameron, J., and Evans, L.R. (2013). Albumin as a versatile platform for drug half-life extension. Biochim. Biophys. Acta-General Subjects *1830*, 5526–5534.

Sproston, N.R., and Ashworth, J.J. (2018). Role of C-reactive protein at sites of inflammation and infection. Front. Immunol. *9*, 754.

Steel, J.C., Waldmann, T.A., and Morris, J.C. (2012). Interleukin-15 biology and its therapeutic implications in cancer. Trends Pharmacological Sciences *33*, 35–41.

Steeland, S., Puimège, L., Vandenbroucke, R.E., Van Hauwermeiren, F., Haustraete, J., Devoogdt, N., Hulpiau, P., Leroux-Roels, G., Laukens, D., Meuleman, P., et al. (2015). Generation and characterization of small single domain antibodies inhibiting human tumor necrosis factor receptor 1. J. Biol. Chem. *290*, 4022–4037.

Steeland, S., Vandenbroucke, R.E., and Libert, C. (2016). Nanobodies as therapeutics: big opportunities for small antibodies. Drug Discov. Today *21*, 1076–1113.

Sudlow, G., Birkett, D.J., and Wade, D.N. (1975). The characterization of two specific drug binding sites on human serum albumin. Mol. Pharmacol. *11*, 824–832.

Sugio, S., Kashima, A., Mochizuki, S., Noda, M., and Kobayashi, K. (1999). Crystal structure of human serum albumin at 2.5 A resolution. Protein Eng. *12*, 439–446.

Sun, Z., Ren, Z., Yang, K., Liu, Z., Cao, S., Deng, S., Xu, L., Liang, Y., Guo, J., Bian, Y., et al. (2019). A next-generation tumor-targeting IL-2 preferentially promotes tumor-infiltrating CD8(+) T-cell response and effective tumor control. Nat. Commun. *10*, 3874.

Tang, G., Peng, L., Baldwin, P.R., Mann, D.S., Jiang, W., Rees, I., and Ludtke, S.J. (2007). EMAN2: an extensible image processing suite for electron microscopy. J. Struct. Biol. *157*, 38–46.

Terryn, S., Francart, A., Lamoral, S., Hultberg, A., Rommelaere, H., Wittelsberger, A., Callewaert, F., Stohr, T., Meerschaert, K., Ottevaere, I., et al. (2014). Protective effect of different anti-rabies virus VHH constructs against rabies disease in mice. PLoS One *9*, e109367.

Tijink, B.M., Laeremans, T., Budde, M., Stigter-van Walsum, M., Dreier, T., de Haard, H.J., Leemans, C.R., and van Dongen, G.A.M.S. (2008). Improved tumor targeting of anti-epidermal growth factor receptor Nanobodies through albumin binding: taking advantage of modular Nanobody technology. Mol. Cancer Ther. *7*, 2288–2297.

Uhlar, C.M., and Whitehead, A.S. (1999). Serum amyloid A, the major vertebrate acute-phase reactant. Eur. J. Biochem. *265*, 501–523.

van Faassen, H., Ryan, S., Henry, K.A., Raphael, S., Yang, Q., Rossotti, M.A., Brunette, E., Jiang, S., Haqqani, A.S., Sulea, T., et al. (2020). Serum albumin-binding V Hs with variable pH sensitivities enable tailored half-life extension of biologics. FASEB J. *34*, 8155–8171.

Van Heeke, G., Allosery, K., De Brabandere, V., De Smedt, T., Detalle, L., and de Fougerolles, A. (2017). Nanobodies® as inhaled biotherapeutics for lung diseases. Pharmacol. Ther. *169*, 47–56.

Vincke, C., Loris, R., Saerens, D., Martinez-Rodriguez, S., Muyldermans, S., and Conrath, K. (2009). General strategy to humanize a camelid single-domain antibody and identification of a universal humanized nanobody scaffold. J. Biol. Chem. *284*, 3273–3284.

Vosjan, M.J.W.D., Vercammen, J., Kolkman, J.A., Stigter-van Walsum, M., Revets, H., and van Dongen, G.A.M.S. (2012). Nanobodies targeting the hepatocyte growth factor: potential new drugs for molecular cancer therapy. Mol. Cancer Ther. *11*, 1017–1025.

Webb, B., and Sali, A. (2014). Comparative protein structure modeling using MODELLER. Curr. Protoc. Bioinformatics *47*, 5 6 1–32.

Weller, M.G. (2016). Quality issues of research antibodies. Anal Chem. Insights *11*, 21–27.

Xiang, Y., Nambulli, S., Xiao, Z., Liu, H., Sang, Z., Duprex, W.P., Schneidman-Duhovny, D., Zhang, C., and Shi, Y. (2020a). Versatile and multivalent nanobodies efficiently neutralize SARS-CoV-2. Science *370*, 1479–1484.

Xiang, Y., Shen, Z., and Shi, Y. (2020b). Chemical cross-linking and mass spectrometric analysis of the endogenous yeast exosome complexes. Methods Mol. Biol. *2062*, 383–400.

Xiang, Y., Sang, Z., Bitton, L., Xu, J., Liu, Y., Schneidman-Duhovny, D., and Shi, Y. (2021). Integrative proteomics identifies thousands of distinct, multi-epitope, and high-affinity nanobodies. Cell Syst. *12*, 220–234.e9.

Yu, C., and Huang, L. (2018). Cross-linking mass spectrometry: an emerging technology for interactomics and structural biology. Anal. Chem. *90*, 144–165.

Zhu, E.F., Gai, S.A., Opel, C.F., Kwan, B.H., Surana, R., Mihm, M.C., Kauke, M.J., Moynihan, K.D., Angelini, A., Williams, R.T., et al. (2015). Synergistic innate and adaptive immune response to combination immunotherapy with anti-tumor antigen antibodies and extended serum half-life IL-2. Cancer Cell *27*, 489–501.

## STAR★METHODS

### KEY RESOURCES TABLE

| REAGENT or RESOURCE | SOURCE | IDENTIFIER |
|---|---|---|
| **Antibodies** | | |
| THE™ His Tag Antibody [HRP], mAb, Mouse | GenScript | A00612; RRID: AB_915573 |
| Biotin anti-mouse CD45 Antibody | Biolegend | 103103; RRID: AB_312968 |
| Biotin anti-mouse CD3 Antibody | Biolegend | 100243; RRID: AB_2563946 |
| Biotin anti-mouse CD8a Antibody | Biolegend | 100703; RRID: AB_312742 |
| Biotin anti-mouse NK-1.1 Antibody | Biolegend | 108703; RRID: AB_313390 |
| **Bacterial and virus strains** | | |
| One Shot™ BL21(DE3) Chemically Competent *E. coli* | Invitrogen | C600003 |
| **Biological samples** | | |
| T-Cell Culture Supplement with ConA (IL-2 Culture Supplement) | Corning | 354115 |
| Recombinant Human IL-2 | PeproTech | 200-02 |
| *InVivo*MAb anti-mouse/human TYRP1/TRP1 (gp75) | BioXCell | BE0151 |
| Corning™ Regular Fetal Bovine Serum 500mL (HI) | Fisher Scientific | MT35011CV |
| **Chemicals, peptides, and recombinant proteins** | | |
| LB Miller Broth | IBI Scientific | 49030 |
| Ampicillin, sodium salt, irradiated | Gibco | 11593027 |
| LB Miller's Agar Powder | Growcells.com | MBPE-3020 |
| Human serum albumin | Prospec | PRO-354 |
| Pierce™ Lys-C Protease, MS Grade | Thermo Fisher | 90051 |
| Sequencing Grade Modified Trypsin | Promega | V5111 |
| Formic Acid, 99+% | Thermo Fisher | PI28905 |
| Water, Optima™ LC/MS Grade | Fisher Scientific | W6-1 |
| Water with 0.1% Formic Acid (v/v), Optima™ LC/MS Grade | Fisher Scientific | LS118-1 |
| Pierce™ Acetonitrile (ACN), LC/MS Grade | Thermo Fisher | 85188 |
| Pierce™ 0.1% Formic Acid (v/v) in Acetonitrile (ACN), LC/MS Grade | Thermo Fisher | 85175 |
| Dulbecco's phosphate buffer saline no Ca 2+, Mg 2+ | Thermo Fisher | 14190250 |
| Pierce™ Protease Inhibitor Tablets, EDTA-free | Thermo Fisher | A32965 |
| Tween® 20 | Sigma | P9416-100ml |
| Dulbecco's Modified Eagle's Medium (DMEM) | ATCC | 30-2002 |
| RPMI-1640 Medium | ATCC | 30-2001 |
| SYPRO™ Orange Protein Gel Stain (5,000X Concentrate in DMSO) | Thermo Fisher | S6650 |
| COLLAGENASE TYPE 4 | Worthington Biochemical | NC9919937 |
| Deoxyribonuclease I | Worthington Biochemical | NC9082558 |
| Trypsin Inhibitor, Soybean | Worthington Biochemical | NC9065058 |
| BioWhittaker™ ACK Lysing Buffer | Lonza | BW10548E |
| Human TruStain FcX™ | Biolegend | 422301 |
| Sodium Pyruvate (100 mM) | Thermo Fisher | 11360070 |
| L-Glutamine Solution, 200 mM | ATCC | 30-2214 |

(*Continued on next page*)

*Continued*

| REAGENT or RESOURCE | SOURCE | IDENTIFIER |
|---|---|---|
| **Critical commercial assays** | | |
| ELISA kit | R & D system | DY990-999 |
| Biacore 3000 kits | GE Healthcare | Multiple |
| Q5® Site-Directed Mutagenesis Kit | NEB | E0554S |
| ToxinEraser™ Endotoxin Removal Kit | GenScript | L00338 |
| ToxinSensor™ Chromogenic LAL Endotoxin Assay Kit | GenScript | L00350 |
| Lipofectamine® 3000 Transfection Reagents | Thermo Fisher | L3000008 |
| Monarch® PCR & DNA Cleanup Kit | NEB | T1030L |
| Monarch® DNA Gel Extraction Kit | NEB | T1020S |
| **Deposited data** | | |
| MS raw data | MassIVE | MSV000086104 |
| **Experimental models: cell lines** | | |
| B16-F10 | ATCC | CRL-6475 |
| CTLL-2 | ATCC | TIB-214 |
| HeLa | N/A | N/A |
| **Experimental models: organisms/strains** | | |
| C57BL/6J | The Jackson Laboratory | 000664 |
| B6.Cg-Tg(FCGRT)32Dcr *Alb*$^{em12Mvw}$ *Fcgrt*$^{tm1Dcr}$/MvwJ | The Jackson Laboratory | 025201 |
| **Oligonucleotides** | | |
| SDM_E400R_F: 5′-GGTGTTCGACcggTTCAAGCCTCTGG-3′ | This paper | N/A |
| SDM_E400R_R: 5′-TTGGCGTAGCACTCGTGA-3′ | This paper | N/A |
| SDM_K383D_F: 5′-AACCCTGGAAgacTGCTGCGCCG-3′ | This paper | N/A |
| SDM_K383D_R: 5′-GTCTCGTAGGTCTTGGCC-3′ | This paper | N/A |
| SDM_bio_del_F: 5′-caccaccatcaccaccattgagtctagac-3′ | This paper | N/A |
| SDM_bio_del_R: 5′-gagtcccagagcaacctgagaggc-3′ | This paper | N/A |
| **Recombinant DNA** | | |
| Multiple Nanobodies in pET-21b(+) vector | Synbio | N/A |
| pMAL-c5x vector (MBP) | General Biosystems | N/A |
| ALB-bio-His (HSA) plasmid | Addgene | 52176 |
| **Software and algorithms** | | |
| Prism GraphPad 7 | GraphPad Software | https://www.graphpad.com/scientific-software/prism/ |
| Web Logo | Crooks et al., 2004 | http://weblogo.threeplusone.com/ |
| Morpheus | Broad Institute | https://software.broadinstitute.org/morpheus/ |
| iTOL | Letunic and Bork, 2007 | https://itol.embl.de/ |
| Clustal Omega | Sievers and Higgins, 2014 | http://www.clustal.org/omega/ |
| MODELLER | Webb and Sali, 2014 | http://salilab.org/modeller |
| IMOD 4.8 | Mastronarde and Held, 2017 | https://bio3d.colorado.edu/imod/ |
| EMAN2 | Tang et al., 2007 | https://blake.bcm.edu/emanwiki/EMAN2 |
| Relion 3.0 | Scheres, 2012 | https://www3.mrc-lmb.cam.ac.uk/relion/index.php/Download_%26_install |
| Chimera | Pettersen et al., 2004 | https://www.cgl.ucsf.edu/chimera/ |
| Chimera X | Pettersen et al., 2021 | https://www.rbvi.ucsf.edu/chimerax/ |

(*Continued on next page*)

*Continued*

| REAGENT or RESOURCE | SOURCE | IDENTIFIER |
|---|---|---|
| MaxQuant version 1.6.1.0 | Cox and Mann, 2008 | https://www.maxquant.org/ |
| pLink 2 | Chen et al., 2019 | http://pfind.ict.ac.cn/software/pLink/ |
| Other | | |
| CNBr - Activated Sepharose™ 4 Fast Flow Affinity Media | GE Healthcare | 17098101 |
| HisPur™ Cobalt Resin | Thermo Fisher | 89966 |

## RESOURCE AVAILABILITY

### Lead contact

Further information and requests for resources and reagents should be directed to and fulfilled by the lead contact, Dr. Yi Shi (yi.shi@pitt.edu).

### Materials availability

Amino acid sequences of nanobodies generated in this paper are available in Data S1. Request for HSA mutant plasmids should be fulfilled by the lead contact Dr. Yi Shi.

### Data and code availability

- Mass spectrometry data of this study have been deposited in MassIVE and are publicly available as of the date of publication. Accession numbers are listed in the key resources table.
- This paper does not report original code.
- Any additional information required to reanalyze the data reported in this paper is available from the lead contact upon request.

## EXPERIMENTAL MODEL AND SUBJECT DETAILS

### Animals

All mouse strains used in this study were obtained from The Jackson Laboratory. B6.Cg-Tg(FCGRT)32Dcr *Alb*$^{em12Mvw}$ *Fcgrt*$^{tm1Dcr}$/MvwJ (JAX #025201) mice were fed on LabDiet® 5K20. 2 male and 1 female mice used in this study were aged 25 weeks before the experiments. Gender is not considered as a confounding factors in this study since grouping is not involved. C57BL/6J (JAX #000664) mice were fed on LabDiet® 5K52. All C57BL/6J mice used in this study were male and aged 8 weeks before the experiments. All animal experimentation was approved by the Institutional Animal Care and Use Committee (IACUC) at University of Pittsburgh.

### Cell lines

All cell lines used in this study were obtained from ATCC and cultured according to the provided protocols. The complete culture medium of CTLL-2 cell line was formulated as 10% FBS, an additional 2 mM L-glutamine, and 1 mM sodium pyruvate in ATCC-formulated RPMI-1640 containing 10% T-STIM with Con A (Corning). The complete medium of B16-F10 cell line is formulated as 10% FBS in ATCC-formulated DMEM.

## METHOD DETAILS

### Nb DNA synthesis and cloning

Nb genes were codon-optimized for expression in *Escherichia coli* and the nucleotides were *in vitro* synthesized (Synbio). The Nb genes were cloned into a pET-21b (+) vector at BamHI and XhoI restriction sites, or a pMAL-c5X vector at BamHI and EcoRI restriction sites.

### Nb purification

Nb DNA constructs were transformed into BL21(DE3) cells and plated on Agar with 50 μg/ml ampicillin at 37°C overnight. A single bacterial colony was picked and cultured in LB broth to reach O.D. at ~450 nm. 0.1 or 0.5 mM IPTG was added to the *E. coli* cell culture for MBP fusion Nbs or his-tagged Nbs induction at 16°C overnight. Cells were then harvested, briefly sonicated, and lysed on ice with a lysis buffer (1xPBS, 150 mM

NaCl, 0.2% TX-100 with protease inhibitor). After lysis, soluble protein extract was collected at 15,000xg for 10 min, and recombinant his-tagged Nbs were purified by His6-Cobalt resin (Thermo) and eluted by imidazole; while MBP-fusion Nbs were purified by amylose resin (NEB) and eluted by maltose. The eluted Nbs were subsequently dialyzed in the dialysis buffer (e.g., 1x DPBS, pH 7.4). A HiLoad 16/600 Superdex 200 pg column (GE Healthcare) on an ÄKTA FPLC protein purification system (GE Healthcare) was used to further purify the Nbs and ensure their monomeric states. The purified Nbs were analyzed by SDS-PAGE. For the animal experiments, excessive endotoxin in the Nbs was removed (below 0.1 EU/dose) by the ToxinEraser Endotoxin Removal column (Genscript) and measured by ToxinSensor Chromogenic LAL Endotoxin Assay Kit (Genscript). The purified Nbs were further sterilized by passing a 0.2 μm filter (Millex) and were stored at −80°C before use.

### ELISA (enzyme-linked immunosorbent assay)

Indirect ELISA was carried out to measure Nb-albumin bindings. Albumin was coated onto a 96-well ELISA plate (R&D system) at 1–10 ng/well in coating buffer (15 mM sodium carbonate, 35 mM sodium bicarbonate, pH 9.6) overnight at 4°C and was blocked with a blocking buffer (DPBS, 0.05% Tween 20, 5% milk) at room temperature for 2 hrs. Nbs were diluted in the blocking buffer and incubated with albumin for 2 hrs. HRP-conjugated secondary antibodies against His-tag (Genscript) were diluted 1:5,000–10,000 and incubated with the well for 1 h at room temperature. After PBST (DPBS, 0.05% Tween 20) washes, the samples were further incubated under dark with freshly prepared w3,3′,5,5′-Tetramethylbenzidine (TMB) substrate for 10 min to develop the signals. After the STOP solution (R&D system), the plates were read at multiple wavelengths (the optical density at 550 nm wavelength subtracted from the density at 450 nm) on a plate reader (Multiskan GO, Thermo Fisher). The relative affinity of each Nb was determined by the average of O.D. readouts. For human and monkey albumin, the relative affinity of each Nb was tested at Nb concentrations of 1 μM, 100 nM, 10 nM, 1 nM, and 100 pM. An average ELISA O.D. of >0.1 was used as the cutoff value to assign albumin binding Nbs. For mouse albumin, relative affinity was tested at one μM and a cutoff O.D. of >1 was used.

### *In vitro* pull-down assay (immunoprecipitation)

Nb or serum albumin was coupled to CNBr-activated sepharose resin (GE Healthcare). For the *in vitro* pull-down assay, different concentrations of Nbs were incubated with the human serum albumin coupled resin. Samples were incubated for 15–30 min at 4°C with gentle agitation. The resin was collected and washed three times with a washing buffer and was boiled in the LDS sample loading buffer (Thermo) before SDS PAGE analysis.

### Nb affinity measurement by surface plasmon resonance (SPR)

Surface plasmon resonance (SPR, Biacore 3000 system, GE Healthcare) was used to measure Nb affinities. Briefly, human serum albumin was immobilized to the flow channels of an activated CM5 sensor-chip. Protein analytes were diluted to 10 μg/mL in 10 mM sodium acetate, pH 4.5, and injected into the SPR system at 5 μL/min for 420 s. The surface was then blocked by 1 M ethanolamine-HCl (pH 8.5). For each Nb analyte, a series of dilution (spanning ~1,000-fold concentration range) was injected in duplicate, with HBS-EP + running buffer (GE-Healthcare) at a flow rate of 20–30 μL/min for 120–180 s, followed by a dissociation time of 10–20 min based on dissociation rate. Between each injection, the sensor chip surface was regenerated twice with a low pH buffer containing ten mM glycine-HCl (pH 1.5–2.5) at a flow rate of 40–50 μL/min for 30 s - 1 min. Binding sensorgrams for each Nb were processed and analyzed using BIAevaluation by fitting with the 1:1 Langmuir model.

### Clustering and phylogenetic tree analysis of $Nb_{HSA}$

A phylogenetic tree was generated by Clustal Omega (Sievers and Higgins, 2014) with the input of unique $Nb_{HSA}$ CDR3 sequences and the adjacent framework sequences (i.e., YYCAA to the N-terminus and WGQG to the C-terminus of CDR3s) to help alignments. The data were plotted by iTOL (Interactive Tree of Life) (Letunic and Bork, 2007). Isoelectric points and hydrophobicities of the CDR3s were calculated using the BioPython library. The sequence logo was plotted using WebLogo (Crooks et al., 2004).

### Thermostability analysis of $Nb_{HSA}$

The thermal stability of $Nb_{HSA}$ was measured by differential scanning fluorimetry (DSF). To prepare DSF samples, $Nb_{HSA}$ were mixed with SYPRO orange dye (Invitrogen) in PBS to reach a final concentration of

2.5–15 μM. The samples were analyzed by a 7900HT Fast Real-Time PCR System (Applied Biosystems) in triplicate. The temperature was programmed to increase from 25°C to 95°C with a ramp rate of 1°C/min to generate the melting curves. The melting point was calculated by first derivatives method (Niesen et al., 2007).

### Chemical cross-linking and mass spectrometry (CXMS)

Nb was incubated with albumin in PBS and 1 mM dithiothreitol (DTT) to allow the formation of the complex. HSA-$Nb_{HSA}$ complexes were cross-linked with 1 mM disuccinimidyl suberate (DSS, ThermoFisher Scientific) for 23 min at 25°C with gentle agitation. The crosslinking reaction was then quenched with 50 mM ammonium bicarbonate (ABC) for 10 min at room temperature. After protein reduction and alkylation, the cross-linked samples were separated by a 4–12% SDS-PAGE gel (NuPAGE, Thermo Fisher). The regions corresponding to the cross-linked species (~130 kDa) were cut and in-gel digested with trypsin and Lys-C as previously described (Shi et al., 2014, 2015; Xiang et al., 2020b). After proteolysis, the peptide mixtures were desalted and analyzed with a nano-LC 1200 (Thermo Fisher) coupled to a Q Exactive™ HF-X Hybrid Quadrupole-Orbitrap™ mass spectrometer (Thermo Fisher). The cross-linked peptides were loaded onto a picoChip column (C18, 3 μm particle size, 300 Å pore size, 50 μm × 10.5 cm; New Objective) and eluted using a 60 min LC gradient: 5% B–8% B, 0–5 min; 8% B – 32% B, 5–45 min; 32% B–100% B, 45–49 min; 100% B, 49 - 54 min; 100% B - 5% B, 54 min–54 min 10 s; 5% B, 54 min 10 s–60 min 10 s; mobile phase A consisted of 0.1% formic acid (FA), and mobile phase B consisted of 0.1% FA in 80% acetonitrile. The QE HF-X instrument was operated in the data-dependent mode, where the top 8 most abundant ions (mass range 380–2,000, charge state 3–7) were fragmented by high-energy collisional dissociation (normalized collision energy 27). The target resolution was 120,000 for MS and 15,000 for MS/MS analyses. The quadrupole isolation window was 1.8 Th, and the maximum injection time for MS/MS was set at 120 ms. After the MS analysis, the data was searched by pLink 2 (Chen et al., 2019) for the identification of cross-linked peptides. The mass accuracy was specified as 10 and 20 p.p.m. for MS and MS/MS, respectively. Other search parameters included cysteine carbamidomethylation as a fixed modification and methionine oxidation as a variable modification. A maximum of three trypsin missed-cleavage sites was allowed. The initial search results were obtained using the default 5% false discovery rate, estimated using a target-decoy search strategy. The cross-link spectra were then manually checked to remove potential false-positive identifications essentially as previously described (Kim et al., 2018; Shi et al., 2014, 2015; Xiang et al., 2020b).

### Integrative structural modeling of HSA-Nb complexes

Structural models for Nbs were obtained using a multi-template comparative modeling protocol of MODELLER (Webb and Sali, 2014). Next, we refined the CDR3 loop and selected the top 5 scoring loop conformations for the downstream docking. Each Nb model was then docked to the HSA structure (PDB: 4g03) by an antibody-antigen docking protocol of PatchDock software that focuses the search to the CDRs (Schneidman-Duhovny et al., 2005) and optimizes CXMS-based distance restraints satisfaction(Schneidman-Duhovny and Wolfson, 2020). A restraint was considered satisfied if the Ca-Ca distance between the cross-linked residues was within 30Å for DSS cross-linkers (Fernandez-Martinez et al., 2016; Shi et al., 2014). The models were then rescored by a statistical potential SOAP (Dong et al., 2013). The antigen interface residues (distance <6Å from Nb atoms) among the 10 best scoring models according to the SOAP score, were used to determine the epitopes. Convergence was measured as the average RMSD among the 10 top-scoring models. Once the epitopes were defined, we clustered the Nbs based on the epitope similarity using hierarchical clustering and displayed the models by Chimera X (Pettersen et al., 2021). The clusters reveal the most immunogenic surface patches on the antigens.

### Size-exclusion chromatography (SEC) and negative stain electron microscopy

HSA and MBP-Nbs were mixed in an HSA: Nb ratio of 1:1.2 and incubated at room temperature for 2 h in PBS and 2 mM DTT. The complexes were analyzed by SEC (Superdex200, GE LifeSciences). HSA and the tetrameric HSA-$Nb_{HSA}$ complex were visualized by transmission electron microscopy (TEM) under negative staining. For TEM analysis, the complexes were digested overnight at 4°C with TEV protease to remove the MBP tag. Protein was diluted to a final concentration of 30 μg/mL (HSA in PBS; HSA-Nb complexes in Tris 20 mM, 200mM NaCl, 3% glycerol) and deposited on carbon-coated CF400-CU grids (EMS) which were freshly glow discharged. After 30 s of incubation, the excessive protein was removed, and the grid was stained with two drops of uranyl acetate 2% w/v. Electron micrographs were recorded in an FEI TECNAI T12 operating at 120 kV with a 2k x 2k Gatan UltraScan 1000. Raw images were converted by IMOD 4.8

(Mastronarde and Held, 2017) and particles were selected using EMAN2 (Tang et al., 2007). Particle processing and 3D reconstruction were done by Relion 3.0 (Scheres, 2012) with several rounds of auto-refine iterations. The final 3D structures were obtained with 4,000 particles for HSA and 21,400 particles for the tetrameric complex. Crystallographic structural models (PDB: 1AO6 and 5VNW) were used for the initial fitting by Chimera (Pettersen et al., 2004).

### Site-directed mutagenesis

An HSA expression plasmid was obtained from Addgene (ALB-bio-His, Plasmid #52176). Rat CD4 d3+4 and enzymatic biotinylation sequence were removed; E400R and K383D point mutations were introduced to the HSA sequence by PCR using the Q5 site-directed mutagenesis kit (NEB). Plasmids bearing wild type HSA and the mutants were transfected to HeLa cells using Lipofectamine 3000 transfection kit (Invitrogen) and Opti-MEM (Gibco) according to the manufacturer's protocol. The cells were cultured overnight before a change of medium to DMEM without FBS supplements to remove BSA. After a 48 h culture at 37°C, 5% $CO_2$, the media expressing HSA were collected and stored at −20°C. The media were analyzed by SDS-PAGE and Western blotting to confirm protein expression.

### MS quantification of Nb pharmacokinetics

600 μg/g of HSA (w:w) was administered in 25-week-old B6.Cg-Tg(FCGRT)32Dcr *Alb*$^{em12Mvw}$ *Fcgrt*$^{tm1Dcr}$/MvwJ mice (JAX, n = 3) by intravenous (*i.v.*) injection three days before the injection of Nbs. A mixture of Nbs including 20 $Nb_{HSA}$ and 2 control Nbs in equal molarity were then injected at 30 μg/g (w:w, day 0). After injections, the whole blood samples were collected from the tail veins of the mice. The blood sampling time for HSA was pre-dose (0 min), 10 min, 24 h, and 48 h. The sampling time for Nb mixture was pre-dose (0 min), 5, 15, 30 min, 1, 2, 4, 8, 16, 24 h, 2, 3, 4, 7, 10, 15, 21 days postdose. Whole blood samples were allowed to clot at room temperature for 30 min and were centrifuged at 4°C, 20,000 × g for 3 min. Serum proteins from the supernatants were collected for the downstream proteomic analysis.

Serum samples were reduced in 8M urea digestion buffer (with 50 mM Ammonium bicarbonate, 5 mM TCEP, and DTT) at 57°C for 1 h, and alkylated in the dark with 30 mM Iodoacetamide for 30 min at room temperature. The samples were in-solution digested with 1:100 (w/w) trypsin and Lys-C at 37°C overnight, with incubation with another bolus of trypsin for 4 h. After proteolysis, the peptide mixtures were desalted and analyzed with an easyLC 1200 device coupled with a Q Exactive™ HF-X Hybrid Quadrupole Orbitrap™ mass spectrometer (Thermo Fisher). Briefly, Nb peptides were loaded onto a picoChip column (C18, 1.9 μm particle size, 120 Å pore size, 75 μm × 25 cm; New Objective) and eluted using a 45-min liquid chromatography gradient (5% B–8% B, 0–3 min; 8% B–42% B, 3–35 min; 42% B–100% B, 35–40 min; 100% B, 40–45 min; mobile phase A consisted of 0.1% formic acid (FA), and mobile phase B consisted of 0.1% FA in 80% acetonitrile (ACN). The flow rate was ~300 nL/min. The QE HF-X instrument was operated in the data-dependent mode, where the top 6 most abundant ions (mass range 300–2,000, charge state 2 - 8) were fragmented by high-energy collisional dissociation (HCD). The target resolution was 120,000 for MS and 60,000 for MS2 analyses. The quadrupole isolation window was 1.8 Th, and the maximum injection time for MS/MS was 120 ms.

Serum proteins including Nbs were first identified by MaxQuant version 1.6.1.0 (Cox and Mann, 2008). Up to 4 unique and specific tryptic peptides with the preference of CDR3-containing peptides with high intensities were selected from each Nb.

For the MS1-based quantification, the area under the curve (AUC) of the selected peptides was calculated from the raw data by using the Xcalibur Qual Browser. For each Nb, AUCs of the selected peptides were averaged to represent the abundance of the Nbs. Selected peptides were validated by MS/MS.

For the MS2-based quantification, an inclusion list of the Nb peptides to be monitored was generated. An LC RT window of −2~+3 min (for a 90-min LC gradient) was used to ensure that all the targeted peptides were included. The instrument was operated in a data-independent model where the targeted peptides were specifically selected for fragmentation (HCD normalized energy 27). Up to 5 abundant fragment ions from each peptide were chosen to increase the specificity of our quantification. AUCs of the fragment ions were calculated using Xcalibur Qual Browser. The relative abundance of Nbs was presented as the median AUC intensities of their respective MS2 fragment ions. It was further normalized based on the total MS1 ion current (TIC) of each LC run. An in-house script was developed to enable the automatic

quantification described above. The samples were analyzed in triplicates. The abundance of serum Nbs in pharmacokinetics analysis was determined by averaging technical and biological replicates; the resulting data were used to fit into a two-phase decay model by Prism GraphPad 7.

### Serum proteomic quantification

1 mg HSA was administered to a B6.Cg-Tg(FCGRT)32Dcr *Alb*$^{em12Mvw}$ *Fcgrt*$^{tm1Dcr}$/MvwJ mouse. Blood samples were collected from the tail vein at the following time: predose, 10 min, 24, 48, 72, 96 h, 7, 10 days. Serum sample preparation and in-solution digestion of serum proteins were processed, as previously mentioned. Peptide samples were analyzed with a nano easyLC 1000 device coupled with a Q Exactive™ HF-X Hybrid Quadrupole Orbitrap™ mass spectrometer (Thermo Fisher). Briefly, Nb peptides were loaded onto an analytic column (1.6 μm particle size, 100 Å pore size, 75 μm × 25 cm; IonOpticks) and eluted using a 90-min liquid chromatography gradient. A QE HF-X instrument was used for analysis. The quadrupole isolation window was 1.6 Th, and the maximum injection time for MS/MS was set at 100 ms. Serum protein levels were quantified using MaxQuant version 1.6.1.0. The resulting raw data were searched against a mouse Uniprot FASTA protein database (December 2018) with fixed modification of carbamidomethylation and variable modifications of methionine oxidation and N-terminal acetylation. Trypsin was set as a digestion enzyme, and a maximal missed cleavage of 2 was allowed. Protein's false discovery rate was set to be 0.01. Minimal peptide length was 7, and maximal peptide mass was 4600 Da. The minimal ratio count of label-free quantification was set to be 2. Serum protein abundance at each time point is derived by averaging ion intensities of 3 technical replicates and normalized based on baseline abundance. Serum proteins were then clustered using the K-means clustering algorithm (K = 10), and heatmap was generated by software Morpheus.

### Purification of duraleukins

hIL-2 (C125A) sequence was fused to C-termini of Nb sequences at the DNA level with a flexible linker $(GGGGS)_2$(Gly-Gly-Gly-Gly-Ser-Gly-Gly-Gly-Gly-Ser). The resulting DNA sequences were synthesized and cloned into pET-21b(+) (Synbio). Plasmids were transformed into BL21(DE3) *E. coli* cells to produce Duraleukins. After IPTG induction, Duraleukins were purified from the cell pallets. Cell pellets containing the inclusion bodies of Duraleukins were washed with a solubilization buffer A (0.1 M Tris, 2% sodium deoxycholate (SDC), 5 mM EDTA, pH 8) and sonicated on ice. Cell lysates were spun down at 12,000 × g for 20 min 4°C. Supernatants were discarded, and the pellets were saved for analysis. Cell pellets were washed with Milli-Q water and spun down at 12,000 × g for 20 min at 4°C. Solubilization buffer B (0.1 M Tris, 6 M guanidine hydrochloride [GuHCl], pH 8) was added to the pallets and incubated for 1 h incubation at room temperature with gentle agitation. After centrifugation 12,000 × g for 20 min at 4°C, the supernatants that contain soluble forms of Duraleukins were collected and subsequently diluted with a Duraleukin refolding buffer (0.1 M Tris, pH 8, the final concentration of 10 mM reduced and 1 mM oxidized glutathione) to a GuHCl concentration of 2 M and a protein concentration of ~0.3 mg/mL. The solutions were then incubated at room temperature for 16 h with gently rotating to allow protein refolding. The insoluble fraction was removed by centrifugation at 16,000 × g for 20 min at 4°C and refolded Duraleukins were obtained in the supernatants. IMAC and FPLC purification, detoxification, and sterilization were performed as described in "Nb purification" section of STAR methods.

### *In vitro* T cell proliferation assay

CTLL-2 cells (ATCC) were cultured according to ATCC's protocol. For the CTLL-2 proliferation assay, cells were grown to a density of 1 × $10^5$cells/mL. Duraleukins or hIL-2 (PeproTech) was added into the wells of a flat-bottom 96-well tissue culture microplate. The final concentration of hIL-2 and Duraleukins was adjusted to 0.01–25 ng/mL and 0.025–50 ng/mL by 2-fold serial dilution. Every concentration group was tested in duplicate. $10^4$ cells were seeded to each well of the plate, and the total volume in each well was 100 μL. The cells were then incubated at 37°C, 5% $CO_2$ for 56 h. 10 μL of WST-1 reagent (Roche) was added to each well and the cells were incubated for another four h. The plate was shaken at 1,000 rpm for 1 min before analysis. A spectrometer read absorbance at 450 nm. 690 nm was used as a reference wavelength. A dose-response curve was fit via nonlinear regression using GraphPad Prism 7.

### Generation and treatment of melanoma mouse model

B16-F10 (ATCC) was cultured according to ATCC's protocol. All C57BL/6J mice (JAX) were aged eight weeks before tumor inoculation. B16-F10 melanoma cells were grown into the logarithmic growth phase

(≤50% confluent), harvested, and adjusted to a concentration of 1 × $10^7$ cells/ml in ice-cold HBSS. Mice were anesthetized with isoflurane and shaved in the middle of the back with a razor. 100 μL ($10^6$) of cells is subcutaneously (s.c.) injected into the middle of the shaved area with a 291/2-G insulin syringe (EXEL). For tumor growth experiments, intraperitoneal injection of DL80 (17 μg), hIL-2 (7.5 μg, PeproTech), TA99 (125 μg, BioXCell), and PBS were done on indicated days. For flow cytometry analysis, a single i.v. administration of DL80 (17 μg) or hIL-2 (7.5 μg) was done on day 12.

### Flow cytometry

The tumor was isolated from the mice (n = 5) 1 or 3 days after a single dose treatment. Cell suspensions were harvested by mechanical dissection and Collagenase IV Cocktail digestion (formulated as 7.4 kU Collagenase Type 4, 53 kU Deoxyribonuclease I, 20 mg Soybean Trypsin Inhibitor in 10 mL cocktail; Worthington Biochemical). The suspensions were passed through 40 μm cell strainers to ensure singularity. Cells were first treated with BioWhittaker ACK lysing buffer (Lonza), followed by TruStain FcX (BioLegend) and stained with antibodies against CD45 (clone 30-F11), CD3 (clone 17A2), CD8a (clone 53–6.7), NK1.1 (clone PK136). All antibodies are purchased from Biolegend. All samples were analyzed on a BD LSRFortessa cell analyzer. Data analysis was performed by Flowjo and Prism GraphPad 7.

## QUANTIFICATION AND STATISTICAL ANALYSIS

Quantification of MS samples was performed by MaxQuant 1.6.1.0 and Xcalibur Qual Browser. Details can be found in STAR methods.

Statistical analysis was performed by Prism GraphPad 7. Details of the statistical analysis performed, exact values of n and what they represent, definitions of the summary statistics used, definitions of significance can be found in the STAR methods of the manuscript.